

Molecular structures of unbound and transcribing RNA polymerase III

Niklas A. Hoffmann¹, Arjen J. Jakobi^{1,2}, María Moreno-Morcillo^{1†}, Sebastian Glatt^{1†}, Jan Kosinski¹, Wim J. H. Hagen¹, Carsten Sachse¹ & Christoph W. Müller¹

Transcription of genes encoding small structured RNAs such as transfer RNAs, spliceosomal U6 small nuclear RNA and ribosomal 5S RNA is carried out by RNA polymerase III (Pol III), the largest yet structurally least characterized eukaryotic RNA polymerase. Here we present the cryo-electron microscopy structures of the *Saccharomyces cerevisiae* Pol III elongating complex at 3.9 Å resolution and the apo Pol III enzyme in two different conformations at 4.6 and 4.7 Å resolution, respectively, which allow the building of a 17-subunit atomic model of Pol III. The reconstructions reveal the precise orientation of the C82–C34–C31 heterotrimer in close proximity to the stalk. The C53–C37 heterodimer positions residues involved in transcription termination close to the non-template DNA strand. In the apo Pol III structures, the stalk adopts different orientations coupled with closed and open conformations of the clamp. Our results provide novel insights into Pol III-specific transcription and the adaptation of Pol III towards its small transcriptional targets.

In eukaryotes, transcription of structured, small RNAs such as tRNAs, spliceosomal U6 small nuclear RNA (snRNA), ribosomal 5S RNA and 7 SL RNA is mediated by RNA polymerase III (Pol III)¹. Transcriptional activity of Pol III is elevated in cancer cells, and the tumour suppressors p53 and Rb and the proto-oncogene Myc directly regulate Pol III-mediated transcription².

Pol III is the largest of the three RNA polymerases, containing 17 subunits with a total molecular weight of 0.7 MDa, while RNA polymerase I (Pol I) and RNA polymerase II (Pol II) comprise 14 and 12 subunits, respectively. The architecture of the 10-subunit core is conserved among all eukaryotic RNA polymerases³. In Pol III it comprises the two largest subunits, C160 and C128, that form the active site. Five additional core subunits ABC27, ABC23, ABC14.5, ABC10 α and ABC10 β are shared between Pol I, Pol II and Pol III. Subunits AC40 and AC19 are common between Pol I and Pol III and are closely related to their Pol II counterparts, Rpb3 and Rpb11. The Pol III core is completed by subunit C11, involved in transcription termination^{4,5} and RNA cleavage activity⁵. Subunit C11 corresponds to subunit A12.2 in Pol I⁶ and both subunits are homologous to a fusion protein that comprises the amino-terminal domain of Pol II subunit Rbp9 and the carboxy-terminal domain of TFIIS⁵.

The Pol III stalk comprises subunits C17 and C25 and is involved in transcription initiation³ and in binding of single-stranded RNA⁷. The C53–C37 heterodimer is involved in transcription initiation and termination^{4,8,9} and is distantly related to Pol I A49–A34.5 and Pol II TFIIF^{3,10,11}. The C53–C37 heterodimer occupies a large density on the Pol III core opposite of the stalk¹² and extends into the DNA-binding cleft as shown by chemical crosslinking^{8,13}. Finally, the C82–C34–C31 heterotrimer forms a stable subcomplex^{14,15} that is positioned on the C160 clamp domain in close proximity to the stalk^{12,16}. The C82–C34–C31 heterotrimer is involved in transcription initiation^{3,17} and recruitment of Pol III to TFIIB^{18,19}. Subunits C82 and C34 in the heterotrimer are distantly related to TFIIE α and TFIIE β , respectively¹⁰, further supporting the hypothesis that during evolution general transcription factors such as TFIIF and TFIIE became stably associated Pol I and Pol III subunits. Maf1 is a global

repressor of Pol III conserved in eukaryotes that under stress conditions becomes dephosphorylated and translocates to the nucleus where it directly binds Pol III^{20,21}.

In the last decade, detailed structural studies of Pol I and Pol II contributed to elucidate basic mechanisms of DNA-dependent RNA transcription^{22–25}. However, structural insight into Pol III-mediated transcription has been limited so far as the highest resolution Pol III structures only extend to 10 Å for apo Pol III²⁶ and to 16.5 Å and 19 Å for the Pol III elongation complex^{21,26}. Here, we present the first atomic structures of apo Pol III and elongating Pol III obtained by single-particle electron cryo-microscopy (cryo-EM). Our reconstructions consolidate biochemical data, allow the detailed comparison with the Pol I and Pol II enzymes, and provide additional insight into Pol III-specific transcription.

Overall architecture of Pol III

Saccharomyces cerevisiae Pol III was purified as previously described²⁷ yielding pure, homogenous and transcriptionally active enzyme (Fig. 1). To shed light onto the Pol III architecture and to further investigate Pol III-mediated transcription, we acquired cryo-EM images of Pol III bound to an assembled transcriptionally active bubble (elongating Pol III, Fig. 1c) and of native unbound Pol III (apo Pol III) on an FEI Titan Krios equipped with a Falcon II direct electron detector (Methods, Extended Data Fig. 1). The final map of elongating Pol III was determined using maximum-likelihood based 3D classification in RELION²⁸ at an average resolution of 3.9 Å (Extended Data Fig. 1), but extends beyond 3.5 Å in the Pol III core (Extended Data Figs 1c, 2 and 3). This electron microscopy density was used to build and refine an atomic model of the complete 17-subunit structure of elongating Pol III (Fig. 1a, Extended Data Fig. 4 and Extended Data Table 1). Representative densities (Fig. 1b, Extended Data Fig. 2) and the relatively isotropic resolution (Extended Data Fig. 1c, Extended Data Table 2) demonstrate that the quality of the cryo-EM density map is comparable to electron density maps of Pol I and Pol II obtained by X-ray crystallography at nominally higher resolutions (Extended Data Fig. 3). The overall architecture of

¹European Molecular Biology Laboratory (EMBL), Structural and Computational Biology Unit, Meyerhofstrasse 1, 69117 Heidelberg, Germany. ²European Molecular Biology Laboratory (EMBL), Hamburg Unit, Notkestrasse 85, 22607 Hamburg, Germany. [†]Present addresses: Spanish National Cancer Research Centre (CNIO), Structural Biology and Biocomputing Programme, 28029 Madrid, Spain (M.M.-M.); Malopolska Centre of Biotechnology, Jagiellonian University, Gronostajowa 7A str, 30-387 Krakow, Poland (S.G.).

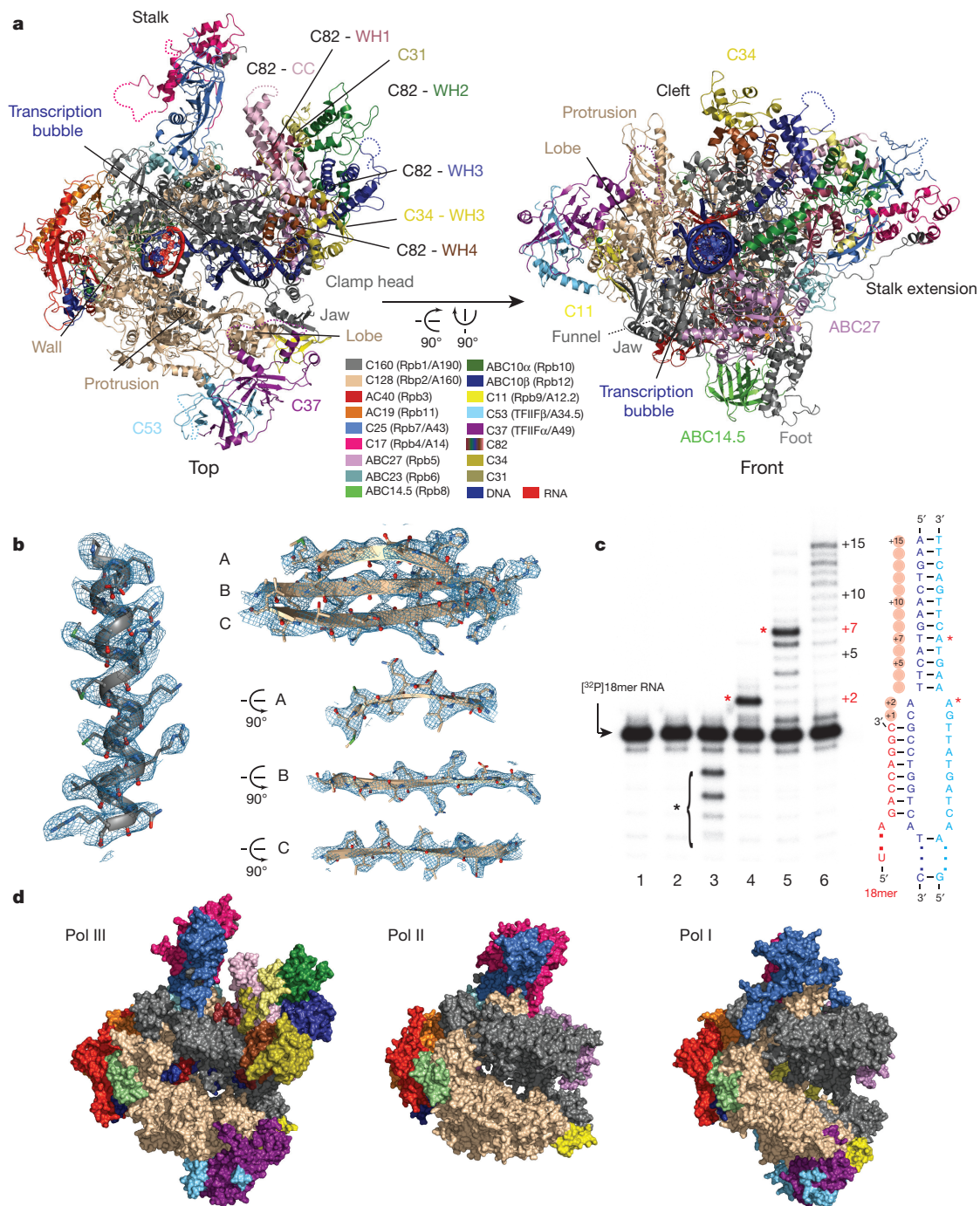


Figure 1 | Cryo-EM structure of RNA polymerase III. **a**, Top and front view of Pol III, individual elements and domains are labelled. Dotted lines indicate regions that are not included in the model. The colour code is presented in the corresponding boxes. **b**, Representative densities of the Pol III core with the fitted model demonstrate the high detail visible in the final cryo-EM structure. **c**, RNA extension assay demonstrates RNA elongation and cleavage activity of Pol III. The transcription bubble used for the activity assays and for the cryo-EM structure determination is depicted at the right (see also Methods). Lane 1, annealed transcription bubble with ³²P-labelled RNA (18mer). Lane 2, with NTP mix. Lane 3,

with Pol III but without NTPs showing the intrinsic RNA cleavage activity of Pol III; cleavage products are denoted by a black asterisk. Lanes 4 and 5, with Pol III and NTPs excluding ATP (Lane 4) or CTP (Lane 5) showing nucleotide-specificity and elongation arrest at +2 (no ATP) or +7 (no CTP) denoted by red asterisks. Lane 6, with Pol III and NTPs, the +15 run-off shows full-length extension. **d**, Surface view of the elongating Pol III structure (this study) compared to Pol I (PDB 4c3i) and Pol II (PDB 1wcm). Homologous subunits in Pol I and Pol II are coloured based on Pol III and as indicated in **a**.

the Pol III core is conserved with respect to Pol I and Pol II (Fig. 1d). However, the clamp head part of subunit C160 is enlarged compared to its Pol I and Pol II counterparts (Extended Data Fig. 5). In addition, C160 contains an extended foot that, unlike Pol I and Pol II, forms a large interface with the shared subunit ABC14.5. Furthermore, a carboxy-terminal extension of C160, unique to Pol III, protrudes

from the core and together with the C160 N terminus contacts the stalk. Similarly, the second largest subunit C128 shows an overall conserved fold, but contains an extended protrusion that increases the depth of the DNA-binding cleft in comparison to Pol I and Pol II (Extended Data Fig. 5). The Pol III cryo-EM structure also includes the Pol III-specific C82–C34–C31 heterotrimer and the C53–C37

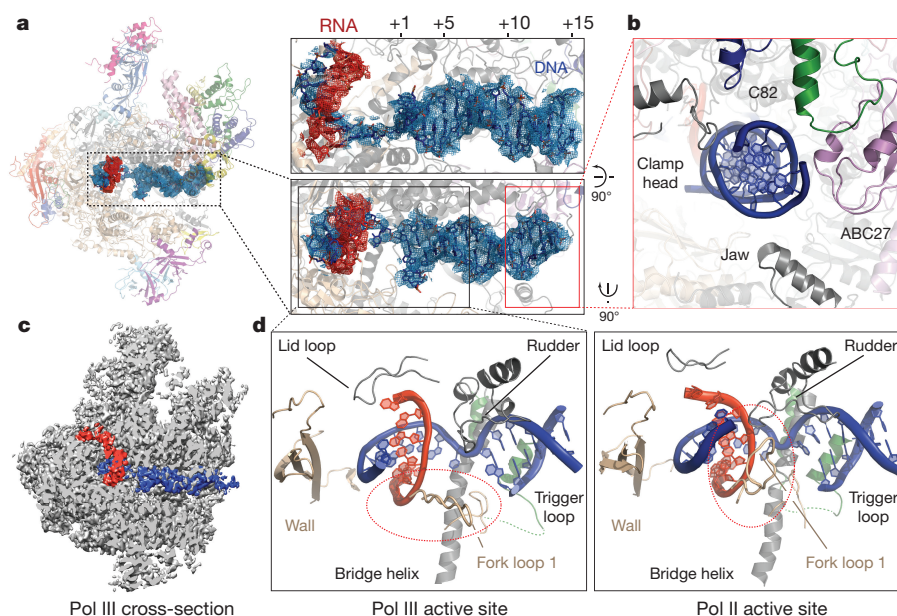


Figure 2 | Transcription of Pol III and association with DNA–RNA duplex. **a**, The left panel shows an elongating Pol III ribbon model with the segmented density of the transcription bubble displayed at 4.5 Å for better visibility. DNA and RNA densities are shown in blue and red, respectively. The transcription bubble is shown in stick representation. The downstream DNA duplex is embedded in the cleft, an eight-base-pair DNA–RNA hybrid was built based on the density. The two right panels show close-ups at two orthogonal views. **b**, The downstream DNA duplex is tightly bound between the jaw (grey), the clamp head (grey), subunit ABC27 (pink) and two C82 WH domains (WH2, green and WH3, blue). **c**, Cross-section of the elongating Pol III density at 3.9 Å with

coloured density corresponding to the transcription bubble. The density for the downstream DNA duplex exceeds even beyond bp +15 in the map, although it is much weaker compared to DNA density in the cleft, thus likely corresponding to an unstably stacked second DNA duplex. **d**, Close-up view of the active site of Pol III (left) and Pol II (right, PDB 1y1w). An extended rudder that points towards a stretch of the protrusion (residues 390–400) and a buried fork loop 1 suggest that the DNA–RNA hybrid in the Pol III core is less tightly bound compared to Pol II (right panel), where fork loop 1 protrudes into the core and together with the rudder and the wall forms a barrier. Similar as in Pol II, the trigger loop is unstructured in Pol III.

heterodimer, both showing several unexpected features as discussed later.

The apo Pol III data set yielded two major 3D classes showing distinct conformations at 4.6 Å and 4.7 Å resolution (Extended Data Fig. 1b, c). One reconstruction is very similar to the elongating Pol III (root mean square deviation (r.m.s.d.) = 0.43 Å_{4,813 C α atoms aligned}), whereas the second reconstruction shows an altered orientation of the stalk, the heterotrimer and a more open cleft resulting in a larger difference with elongating Pol III (r.m.s.d. = 2.73 Å_{4,795 C α atoms aligned}). The two apo Pol III conformations presumably result from ‘closed’ and ‘open’ states of the clamp domain as discussed below (Extended Data Fig. 6a–c).

A narrow cleft encloses DNA

In both apo Pol III and the elongating Pol III structures we observe a characteristic narrower cleft in comparison to Pol I and Pol II (Extended Data Fig. 6d). The DNA duplex is embedded into the Pol III cleft and extends from downstream base pair (bp) +14 towards the active site until the upstream bp –9 (Fig. 2a). The DNA duplex is anchored between the jaw and lobe domains and the oppositely positioned extended clamp head. In addition, the WH2 and WH3 domains of C82 (see below) lie in close proximity and further stabilize downstream DNA (Fig. 2b). Subunit ABC27 completes this enclosure by inserting a proline-containing loop into the minor groove between bps +11 to +14, thus threading the DNA duplex towards the active centre. In the crystal structure of elongating Pol II bound to a transcription bubble that comprises upstream and downstream DNA duplexes (53-mer DNA oligonucleotides)²⁹, the proline-containing loop also protrudes into the minor groove of downstream DNA, while upstream DNA interacts with a hairpin-loop/wedge in Pol II subunit Rbp2 (residues 862–874) also present in Pol III subunit C128 (residues 794–806) as well as in Pol I. Global recognition of upstream and downstream DNA

therefore appears to be conserved among the three eukaryotic RNA polymerases.

The template DNA strand unwinds at bp +2 and a characteristic A-type DNA–RNA hybrid forms at positions –1 to –9 (Fig. 2a). Additional density in the RNA exit channel likely corresponds to the emerging and thus more flexible single-stranded RNA (Fig. 2c). No clear density for upstream DNA is visible, indicating flexibility of the emerging duplex. Another noticeable feature is the strong density of the downstream DNA double strand in comparison to the much weaker density for the DNA–RNA duplex (Fig. 2a–c). This is in contrast to the Pol II elongation complex, where both densities are of equal quality^{29–31}. Remarkably, the DNA–RNA duplex is tightly associated with the Pol II elongation complex between the wall and fork loop 1/rudder, whereas in Pol III the rudder and fork loop 1 reach towards the protrusion, thereby reducing the association of the DNA–RNA hybrid with the Pol III active centre (Fig. 2d). While the DNA–RNA hybrid appears to be only loosely associated with the active site, we observe a tight enclosure of the downstream DNA duplex at the entrance of the DNA-binding cleft.

Pol III heterotrimer protrudes into the cleft

Although the crystal structure of the human C82 orthologue hRPC62 (ref. 32) is available, its integration into the C82–C34–C31 heterotrimer and the precise orientation of the heterotrimer within the complete Pol III enzyme could not be clarified by previous cryo-EM reconstructions owing to their limited resolution^{12,21,26}. In addition, the functional roles of the seven winged-helix (WH) domains present in subunits C82 and C34 and often found in transcription factors as DNA-binding or protein–protein interaction modules³³ are still poorly understood. Our cryo-EM structure shows how the heterotrimer packs onto the clamp head by forming a large, hydrophobic interface through various WH domains (C82–WH1/WH4 and C34–WH3; Fig. 3). In this case the WH domains serve as protein–protein interacting domains, although they

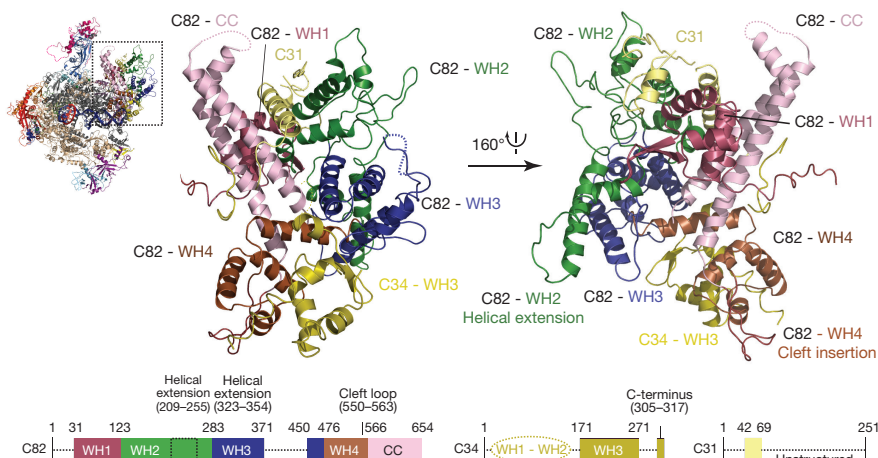


Figure 3 | Architecture of the Pol III-specific heterotrimer. The panel shows the C82–C34–C31 heterotrimer as ribbon representation in top (left) and bottom (right) view. Schematic representations of C82 (left), C34 (middle) and C31 (right) depict domain boundaries. Structured and disordered regions are marked with solid and dotted lines, respectively.

might still contact DNA during open complex formation in the transcription initiation process. The coiled-coil domain of C82 protrudes towards the stalk and the remaining C82-WH2 and WH3 are facing away from the core. Notably, C82-WH2 and C82-WH3 align with the clamp head to reach around bp +15 towards downstream DNA. Furthermore, an additional long ‘cleft loop’ extending from C82-WH4 passes through a canyon in the clamp head into the DNA-binding cleft close to DNA bp +7 (Extended Data Fig. 7a). Subunit C34 comprises three WH domains that span from C82 towards the protrusion crossing the DNA-binding cleft¹⁶. TFIIE α/β also possesses three WH domains and, in the cryo-EM structure of the human Pol II pre-initiation complex, crosses the DNA-binding cleft³⁴. The two N-terminal C34 WH domains are not visible in the Pol III cryo-EM density like the A49 tandem WH domain in the Pol I crystal structure^{24,25}, while the third WH domain tightly associates with C82 and is located at the periphery of the heterotrimer. The C34 C-terminal region following the third WH domain passes the C82-WH4 and contacts the C82 coiled-coil domain (Fig. 3). The third subunit of the heterotrimer, namely C31, was predicted to be largely unstructured and associated between C82 and the stalk, as shown by crosslinking analysis¹⁶. However, we were able to build a mainly helical element of C31 (residues 42–69), demonstrating that C31 extends along the surface from the C34 C terminus towards C82-WH4 over the C82 coiled-coil domain to reach the stalk, where it becomes disordered. Additional density close to the interface of C82-WH1 and WH2 and between the heterotrimer and the stalk is most likely to correspond to C-terminal stretches of C31, but no sequence could be unambiguously assigned to it (Extended Data Fig. 7b). Nevertheless, the topology of C31 and the extended interaction interface with at least three WH domains, the C82 coiled-coil domain and the stalk confirm the previously reported role of C31 in connecting the heterotrimer to the Pol III core and stalk^{17,35,36}.

Transcription termination by Pol III heterodimer

Previous electron microscopy and crosslinking studies of Pol III and the C53–C37 subcomplex positioned a conserved dimerization module at the lobe of Pol III^{12,13,21,26} similar to TFIIF and A49–A34.5 in Pol II³⁷ and Pol I^{24,25}, respectively. On the other hand, extensions of C53 and C37 crosslink close to the active site, the stalk and the heterotrimer^{8,13,16}. Our structure better characterizes the interaction network of the C53–C37 heterodimer with other Pol III subunits. Notably, C37 shows an extended contact surface with C11 and the cleft when compared to TFIIF α and A49 (Fig. 4a), consistent with its proposed role in C11 association with the core⁹.

Our cryo-EM structure also rationalizes the role of the C53–C37 heterodimer in Pol III transcription termination that only requires a stretch of 5–7 thymines in the non-template DNA strand for efficient transcription termination³⁸. Subunit C37 extends towards the DNA-binding cleft where it positions a flexible loop (residues 197–224) that

has been shown to contact C34 and the Pol III-specific TFIIB subunit Bdp1^{13,39} before folding back into a helix (residues 230–240; Extended Data Fig. 8a). Deleting the five residues (R226, L227, T228, G229, S230) leading into this helix produces a terminator read-through phenotype in *S. cerevisiae*⁴, and in *Schizosaccharomyces pombe* the corresponding region was identified as a hotspot for terminator read-through mutations⁴⁰. The same residues have also been cross-linked to C128 (ref. 13) and in the cryo-EM structure are packed onto a section of the C128 lobe that when deleted also results in a termination read-through phenotype⁴¹. In addition, these five residues are in close proximity to the non-template DNA strand that is flexible in the Pol III structure (Extended Data Fig. 8a). Direct interactions between subunit C37 presumably involve these five residues and the first four thymines of the non-template DNA strand and result in a conformational switch of Pol III towards a metastable pre-termination complex, while the presence of a fifth thymine results in transcription termination⁴. In contrast, Pol I and Pol II require additional *cis*- and/or *trans*-acting factors for transcription termination⁴², and accordingly TFIIF or A49–A34.5 do not possess similar features (Fig. 4a).

The C terminus of C37 folds back and forms a hydrophobic interface with the C53 and C37 core consistent with the crucial role of the C37 C terminus in assembling and stabilizing the C53–C37 heterodimer⁹. C53 is located below the lobe and extension 2 and its C-terminal dimerization domain is indeed tightly associated with the C37 dimerization domain (Fig. 4a). The remaining 270 residues of the N-terminal region of C53 are flexible and could not be attributed to any density, although crosslinking experiments suggest that they are involved in a complex interaction network^{8,13}. Interestingly, weak (but continuous) density in the cleft between C11 and C37 could be identified as a part of C53 based on specific photo-crosslinks¹³, although the density is too weak for model building and sequence assignment (Extended Data Fig. 8b). This observation implies that the N-terminal extension of C53 travels from the C160 funnel back to the periphery of the heterodimer in close proximity to the previously described C37–C11 interacting region before moving towards the cleft, the stalk and the heterotrimer^{8,13,16}.

The TFIIS-like domain of C11 is flexible

The core subunit C11 is responsible for the intrinsic RNA cleavage activity of Pol III⁴³ that is likely to be mediated by its conserved TFIIS-like domain⁵. Notably, the orthologous Pol I subunit A12.2 also contains a C-terminal TFIIS-like domain that associates to the active site^{24,25}. Both C11 and A12.2 also harbour a conserved N-terminal Zn-binding domain with high homology to Pol II Rbp9. The N-terminal Rbp9-like domain of C11 is anchored between C37, the C128 lobe domain and the jaw domain of subunit C160 at a similar position as the N-terminal domains of Rbp9 and A12.2 (Fig. 4b). In contrast, density corresponding to the C-terminal TFIIS-like domain was not observed in the elongating Pol III structure, but was only identified in both apo Pol III structures

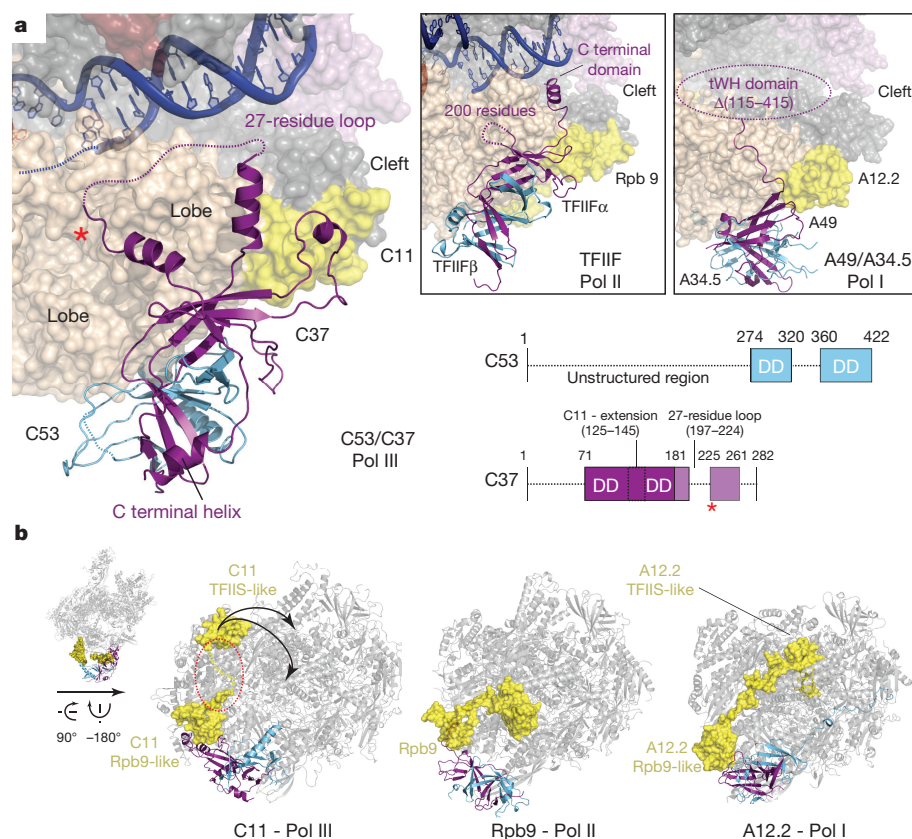


Figure 4 | Architecture and Pol III-specific function of the C53–C37 heterodimer and C11. **a**, Model of the Pol III C53–C37 heterodimer shown in ribbon representation bound to the Pol III core (left), Pol II homologue TFIIFα/β bound to the Pol II core (centre, PDB 4v1n) and Pol I homologue A49–A34.5 bound to the Pol I core (right, PDB 4c3i). The red asterisk (left panel) marks the position of the five residues that upon deletion lead to a terminator read-through phenotype¹³. Schematic representations of C53 and C37 show the domain boundaries of the dimerization domain (DD) and additional elements. Dotted lines indicate unstructured regions. **b**, Conformation of subunit C11 in Pol III (left), subunit Rpb9 in Pol II (middle), and subunit A12.2 in Pol I. Subunits C11, Rpb9 and A12.2 are depicted with yellow surface rendering; C53–C37, TFIIFα/β and A49–A34.5 are depicted in ribbon representation, all other subunits are coloured in grey. Arrows indicate the potential movement of the C11 C-terminal TFIIS domain, the red dotted circle indicates the linker that connects the C11 N- and C-terminal domains.

where it occupies a cleft between Rpb5 and the C160 funnel as observed at a low density threshold (Extended Data Fig. 7c). The position of the C11 C-terminal domain is far away from the position of the corresponding A12.2 C-terminal domain, suggesting that the C11 C-terminal domain is mobile and only temporally recruited to the catalytic centre (in analogy to TFIIS in Pol II). A long linker (residues 37–61) that connects both domains presumably accounts for the required mobility (Fig. 4b). C11 mutations at the extended interface between C37 and C11 N-terminal domain induce terminator read-through transcripts, while mutations of the C-terminal domain of C11 affect RNA 3' cleavage, reflecting the involvement of the flexibly linked N- and C-terminal domains of C11 in two termination-related, yet distinct activities⁴⁴.

Pol III stalk relays conformational changes

The Pol III stalk subunits C25 and C17 are homologous to Pol II Rpb7–Rpb4 and Pol I A43–A14 (refs 7, 36). Consistent with previous low-resolution electron microscopy studies^{12,21,26}, the Pol III cryo-EM structure confirms that the closed HDRC domain fold observed in the *S. pombe* C25–C17 heterodimer⁴⁵ (PDB 3ayh) describes the conformation of the stalk on active Pol III most appropriately. Furthermore, we see a tight interaction network of the Pol III stalk and the C160 N- and C-terminal extensions, the latter contacting and positioning the C17 HDRC domain

on C25 (Extended Data Fig. 8c). This leads to a tight anchoring of the stalk to the core, which is additionally strengthened by the Pol III-specific helix of C25 that extends from the stalk and contacts the clamp.

Remarkably, the open and closed clamp conformations of apo Pol III (Extended Data Fig. 6b) demonstrate two structurally distinct conformations of the stalk, the clamp head and the heterotrimer (Fig. 5). A flexible clamp has been also reported in the bacterial RNA polymerase, where it was shown that the clamp is predominantly open in the unbound conformation, then closes during initiation and elongation⁴⁶. Furthermore, the archaeal RNA polymerase and Pol II contain a flexible clamp and in both systems the status of the clamp is associated with the stalk^{30,34,47}. In contrast to archaeal RNA polymerase and Pol II, in Pol III the clamp movement is less pronounced, resulting in a narrower Pol III cleft compared to other RNA polymerases even in the open clamp conformation (Extended Data Fig. 6c, d). Here, we show both clamp conformations in Pol III visualized from the same sample and speculate that a moving stalk in Pol III can mediate the observed conformational changes. The open clamp conformation opens the cleft and Pol III could thus better associate with target DNA, whereas a transition to the closed clamp positions the heterotrimer next to the unwound DNA and could enable C82 and C34-mediated promoter opening and subsequent elongation.

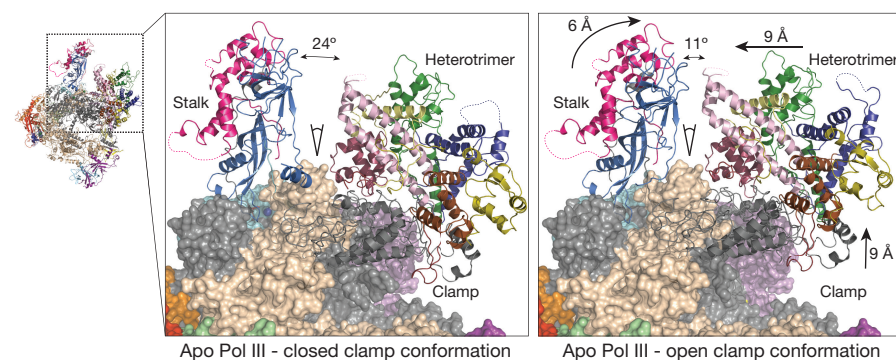


Figure 5 | Conformational changes in apo Pol III. 'Closed clamp' (left) and 'open clamp' (right) conformations of apo Pol III. The C82–C34–C31 heterotrimer, the stalk and the clamp are shown in ribbon representation, the core in surface representation. Arrows in the right panel and corresponding values indicate movements of the stalk, the heterotrimer and the clamp head relative to the closed clamp state.

Online Content Methods, along with any additional Extended Data display items and Source Data, are available in the online version of the paper; references unique to these sections appear only in the online paper.

Received 29 July; accepted 13 October 2015.

Published online 25 November 2015.

- Dieci, G., Fiorino, G., Castelnovo, M., Teichmann, M. & Pagano, A. The expanding RNA polymerase III transcriptome. *Trends Genet.* **23**, 614–622 (2007).
- White, R. J. RNA polymerases I and III, non-coding RNAs and cancer. *Trends Genet.* **24**, 622–629 (2008).
- Vannini, A. & Cramer, P. Conservation between the RNA polymerase I, II, and III transcription initiation machineries. *Mol. Cell* **45**, 439–446 (2012).
- Arimbasseri, A. G. & Maraia, R. J. Mechanism of transcription termination by RNA polymerase III utilizes a non-template strand sequence-specific signal element. *Mol. Cell* **58**, 1124–1132 (2015).
- Chédin, S., Riva, M., Schultz, P., Sentenac, A. & Carles, C. The RNA cleavage activity of RNA polymerase III is mediated by an essential TFIIIS-like subunit and is important for transcription termination. *Genes Dev.* **12**, 3857–3871 (1998).
- Werner, M., Thuriaux, P. & Soutourina, J. Structure-function analysis of RNA polymerases I and III. *Curr. Opin. Struct. Biol.* **19**, 740–745 (2009).
- Jasiak, A. J., Armache, K. J., Martens, B., Jansen, R. P. & Cramer, P. Structural biology of RNA polymerase III: subcomplex C17/25 X-ray structure and 11 subunit enzyme model. *Mol. Cell* **23**, 71–81 (2006).
- Kassavetis, G. A., Prakash, P. & Shim, E. The C53/C37 subcomplex of RNA polymerase III lies near the active site and participates in promoter opening. *J. Biol. Chem.* **285**, 2695–2706 (2010).
- Landrieux, E. et al. A subcomplex of RNA polymerase III subunits involved in transcription termination and reinitiation. *EMBO J.* **25**, 118–128 (2006).
- Carter, R. & Drouin, G. The increase in the number of subunits in eukaryotic RNA polymerase III relative to RNA polymerase II is due to the permanent recruitment of general transcription factors. *Mol. Biol. Evol.* **27**, 1035–1043 (2010).
- Geiger, S. R. et al. RNA polymerase I contains a TFIIIF-related DNA-binding subcomplex. *Mol. Cell* **39**, 583–594 (2010).
- Fernández-Tornero, C. et al. Insights into transcription initiation and termination from the electron microscopy structure of yeast RNA polymerase III. *Mol. Cell* **25**, 813–823 (2007).
- Wu, C. C., Lin, Y. C. & Chen, H. T. The TFIIIF-like Rpc37/53 dimer lies at the center of a protein network to connect TFIIIC, Bdp1, and the RNA polymerase III active center. *Mol. Cell. Biol.* **31**, 2715–2728 (2011).
- Lane, L. A. et al. Mass spectrometry reveals stable modules in holo and apo RNA polymerases I and III. *Structure* **19**, 90–100 (2011).
- Wang, Z. & Roeder, R. G. Three human RNA polymerase III-specific subunits form a subcomplex with a selective function in specific transcription initiation. *Genes Dev.* **11**, 1315–1326 (1997).
- Wu, C. C. et al. RNA polymerase III subunit architecture and implications for open promoter complex formation. *Proc. Natl Acad. Sci. USA* **109**, 19232–19237 (2012).
- Thuillier, V., Stettler, S., Sentenac, A., Thuriaux, P. & Werner, M. A mutation in the C31 subunit of *Saccharomyces cerevisiae* RNA polymerase III affects transcription initiation. *EMBO J.* **14**, 351–359 (1995).
- Brun, I., Sentenac, A. & Werner, M. Dual role of the C34 subunit of RNA polymerase III in transcription initiation. *EMBO J.* **16**, 5730–5741 (1997).
- Khoo, S. K., Wu, C. C., Lin, Y. C., Lee, J. C. & Chen, H. T. Mapping the protein interaction network for TFIIIF-related factor Brf1 in the RNA polymerase III preinitiation complex. *Mol. Cell. Biol.* **34**, 551–559 (2014).
- Boguta, M. Maf1, a general negative regulator of RNA polymerase III in yeast. *Biochim. Biophys. Acta* **1829**, 376–384 (2013).
- Vannini, A. et al. Molecular basis of RNA polymerase III transcription repression by Maf1. *Cell* **143**, 59–70 (2010).
- Sainsbury, S., Bernecky, C. & Cramer, P. Structural basis of transcription initiation by RNA polymerase II. *Nature Rev. Mol. Cell Biol.* **16**, 129–143 (2015).
- Svetlov, V. & Nudler, E. Basic mechanism of transcription by RNA polymerase II. *Biochim. Biophys. Acta* **1829**, 20–28 (2013).
- Fernández-Tornero, C. et al. Crystal structure of the 14-subunit RNA polymerase I. *Nature* **502**, 644–649 (2013).
- Engel, C., Sainsbury, S., Cheung, A. C., Kostrewa, D. & Cramer, P. RNA polymerase I structure and transcription regulation. *Nature* **502**, 650–655 (2013).
- Fernández-Tornero, C. et al. Conformational flexibility of RNA polymerase III during transcriptional elongation. *EMBO J.* **29**, 3762–3772 (2010).
- Moreno-Morcillo, M. et al. Solving the RNA polymerase I structural puzzle. *Acta Crystallogr. D* **70**, 2570–2582 (2014).
- Scheres, S. H. RELION: implementation of a Bayesian approach to cryo-EM structure determination. *J. Struct. Biol.* **180**, 519–530 (2012).
- Barnes, C. O. et al. Crystal structure of a transcribing RNA polymerase II complex reveals a complete transcription bubble. *Mol. Cell* **59**, 258–269 (2015).
- Gnatt, A. L., Cramer, P., Fu, J., Bushnell, D. A. & Kornberg, R. D. Structural basis of transcription: an RNA polymerase II elongation complex at 3.3 Å resolution. *Science* **292**, 1876–1882 (2001).
- Kettenberger, H., Armache, K. J. & Cramer, P. Complete RNA polymerase II elongation complex structure and its interactions with NTP and TFIIIS. *Mol. Cell* **16**, 955–965 (2004).
- Lefèvre, S. et al. Structure-function analysis of hRPC62 provides insights into RNA polymerase III transcription initiation. *Nature Struct. Mol. Biol.* **18**, 352–358 (2011).
- Aravind, L., Anantharaman, V., Balaji, S., Babu, M. M. & Iyer, L. M. The many faces of the helix-turn-helix domain: transcription regulation and beyond. *FEMS Microbiol. Rev.* **29**, 231–262 (2005).
- He, Y., Fang, J., Taatjes, D. J. & Nogales, E. Structural visualization of key steps in human transcription initiation. *Nature* **495**, 481–486 (2013).
- Schramm, L. & Hernandez, N. Recruitment of RNA polymerase III to its target promoters. *Genes Dev.* **16**, 2593–2620 (2002).
- Ferri, M. L. et al. A novel subunit of yeast RNA polymerase III interacts with the TFIIIF-related domain of TFIIIB70. *Mol. Cell. Biol.* **20**, 488–495 (2000).
- Plaschka, C. et al. Architecture of the RNA polymerase II-Mediator core initiation complex. *Nature* **518**, 376–380 (2015).
- Arimbasseri, A. G., Rijal, K. & Maraia, R. J. Comparative overview of RNA polymerase II and III transcription cycles, with focus on RNA polymerase III termination and reinitiation. *Transcription* **5**, e27369 (2014).
- Hu, H. L., Wu, C. C., Lee, J. C. & Chen, H. T. A region of Bdp1 necessary for transcription initiation that is located within the RNA polymerase III active site cleft. *Mol. Cell. Biol.* **35**, 2831–2840 (2015).
- Rijal, K. & Maraia, R. J. RNA polymerase III mutants in TFIIIF-like C37 that cause terminator readthrough with no decrease in transcription output. *Nucleic Acids Res.* **41**, 139–155 (2013).
- Shaaban, S. A., Krupp, B. M. & Hall, B. D. Termination-altering mutations in the second-largest subunit of yeast RNA polymerase III. *Mol. Cell. Biol.* **15**, 1467–1478 (1995).
- Richard, P. & Manley, J. L. Transcription termination by nuclear RNA polymerases. *Genes Dev.* **23**, 1247–1269 (2009).
- Whitehall, S. K., Bardeleben, C. & Kassavetis, G. A. Hydrolytic cleavage of nascent RNA in RNA polymerase III ternary transcription complexes. *J. Biol. Chem.* **269**, 2299–2306 (1994).
- Iben, J. R. et al. Point mutations in the Rpb9-homologous domain of Rpc11 that impair transcription termination by RNA polymerase III. *Nucleic Acids Res.* **39**, 6100–6113 (2011).
- Ehara, H., Sekine, S. & Yokoyama, S. Crystal structure of the C17/25 subcomplex from *Schizosaccharomyces pombe* RNA polymerase III. *Protein Sci.* **20**, 1558–1565 (2011).
- Chakraborty, A. et al. Opening and closing of the bacterial RNA polymerase clamp. *Science* **337**, 591–595 (2012).
- Jun, S. H. et al. The X-ray crystal structure of the euryarchaeal RNA polymerase in an open-clamp configuration. *Nature Commun.* **5**, 5132 (2014).

Acknowledgements We thank Y. Sadian, H. Grötsch and R. Wetzel for help in Pol III purification. We are grateful to F. Thommen and M. Wahlers for set-up and maintenance of the high-performance computational environment of RELION. We acknowledge F. Schur, S. Fromm, C. Bertipaglia, M. Beck and G. Hofhaus for helpful advice regarding sample preparation and image processing. We also thank the ‘Fermentation et culture de microorganismes’ (IFR88, CNRS, Marseille). M.M.-M. and A.J.J. were supported by Marie-Sklodowska-Curie fellowships (FP7-PEOPLE-2011IEF301002, PIF-GA-2012-331285). N.A.H. acknowledges support by the EMBL International PhD program, A.J.J. and J.K. by postdoctoral fellowships from the EMBL Interdisciplinary Postdoc Program (EIPOD) under Marie Curie COFUND actions (PCOFUND-GA-2008-229597) and C.W.M. by an ERC Advanced Grant (ERC-2013-AdG340964-POL1PIC).

Author Contributions C.W.M. and C.S. initiated and supervised the project. N.A.H. established and performed Pol III experiments with input from C.W.M., S.G. and M.M.-M.; N.A.H., C.S. and W.J.H.H. established the grid freezing and acquisition parameters, N.A.H. and W.J.H.H. collected all cryo-EM data. N.A.H., M.M.-M. and A.J.J. built the initial model. N.A.H., A.J.J. and C.S. analysed cryo-EM data. J.K. performed homology modelling and alignments, A.J.J. established the refinement protocol. A.J.J. and N.A.H. optimized the refinement protocol and revised the models. N.A.H., A.J.J., S.G., M.M.-M., C.S. and C.W.M. wrote the manuscript with input from all authors.

Author Information The 3.9 Å cryo-EM map of elongating Pol III and the two maps of apo Pol III have been deposited in the Electron Microscopy Data Bank with accession codes EMD-3178 (elongating Pol III) and EMD-3179 (‘closed clamp’ apo Pol III) EMD-3180 (‘open clamp’ apo Pol III). The coordinates of the corresponding atomic models have been deposited in the Protein Data Bank under accession code 5fj8 (elongating Pol III) and 5fj9 (‘closed clamp’ apo Pol III), 5fja (‘open clamp’ apo Pol III). Reprints and permissions information is available at www.nature.com/reprints. The authors declare no competing financial interests. Readers are welcome to comment on the online version of the paper. Correspondence and requests for materials should be addressed to C.S. (carsten.sachse@embl.de) or C.W.M. (christoph.mueller@embl.de).

METHODS

Sample preparation. The 38-nucleotide template DNA strand (5'-AAGTCAAG TACTTACGCCTGGTCACTTACTAGTACTGCC-3'), non-template DNA strand (5'-GGCAGTACTAGTAACTAGTATTGAAAGTACTTGA-3') and the 18-nucleotide RNA (5'-UAUGCAUAAAGACCAGGC-3') were designed as previously described³¹, except that a two-nucleotide overhang on both ends and one GC base pair was removed. HPLC grade single-stranded oligonucleotides (Eurofins MWG Synthesis GmbH) were diluted in 15 mM Tris, pH 7.5, 150 mM (NH₄)₂SO₄. Template and non-template strands were heated to 95 °C and slowly cooled to room temperature allowing formation of the 11-nucleotide mismatch double-stranded DNA. In a second step, RNA was added, the mixture heated to 45 °C, and slowly cooled to 4 °C. Finally, 5 mM MgCl₂ and 10 mM DTT were added to the annealed transcription bubble.

Pol III was purified endogenously from *Saccharomyces cerevisiae* as previously described²⁷. For apo Pol III, the buffer was exchanged to EM-buffer (15 mM Tris pH 7.5, 150 mM (NH₄)₂SO₄, 10 mM DTT) and diluted to 0.2 mg ml⁻¹ for grid freezing. To form the Pol III elongation complex, the buffer was exchanged to EM-buffer and 5 mM MgCl₂ were added. Pol III was then diluted to 1 mg ml⁻¹ and incubated with 5× excess of transcription bubble for 1 h at 7 °C. The elongating Pol III complexes were then diluted 5 fold for grid freezing.

RNA extension assay. Labelling of the RNA and annealing was performed as previously described²⁴ except that the full transcription bubble (see above) was used as template. An excess of transcription bubble was incubated with Pol III in EM-buffer for 1 h at 4 °C. The RNA elongation was initiated by addition of NTPs in EM-buffer with additional 10 mM MgCl₂ at 28 °C for 20 min. The reaction was stopped by adding 1 × 8 M urea loading buffer and subsequent heating to 95 °C for 5 min. The samples were analysed on a denaturing polyacrylamide gel (17% PAGE, 7 M urea) using a FLA7000 phosphorimager (Fujifilm).

Electron microscopy. A total of 2.5 µl of 0.2 mg ml⁻¹ Pol III and ~0.2 mg ml⁻¹ elongating Pol III were applied to glow-discharged Quantifoil grids (400 mesh holey carbon 1.2/1.3 copper for elongating Pol III and molybdenum for apo Pol III) using an FEI Vitrobot at 95% humidity and 20 °C (Vitrobot Mark III, FEI). The sample was incubated for 15 s on the grid before blotting for 9 s (double-sided, blot force 3) and immediately flash-frozen in liquid ethane.

Micrographs were acquired at 300 kV using an FEI Titan Krios equipped with a Falcon II direct detector at a magnification of 75,000, corresponding to a pixel size of 1.084 Å. Image acquisition was performed with EPU Software (FEI Eindhoven, Netherlands) and micrographs were collected at an under-focus varying between 1.4 and 4.2 µm. We collected a total of seven frames accumulating to a dose of 42 e⁻ Å⁻² (apo Pol III) and 45.5 e⁻ Å⁻² (elongating Pol III) over 2.0 s exposure for apo Pol III and 1.6 s for elongating Pol III. In total, 2,398 and 2,639 micrographs were collected for elongating Pol III and for apo Pol III, respectively.

Image processing. The seven frame micrographs were aligned using MOTIONCORR⁴⁸. The resulting frame stacks and total exposure images (7 frame sums) were used for further processing. The contrast-transfer function of the micrographs was determined using CTFFIND3 (ref. 49) and Thon rings were manually inspected for astigmatism. Particle picking was performed on 20 Å low-pass filtered micrographs (Extended Data Fig. 1a). Initially, a subset of 100 micrographs was chosen from the elongating Pol III data set and a total of 14,942 particles were selected manually using EMAN2 boxer swarm tool⁵⁰. 2D classes from RELION²⁸ obtained with the subset were used as templates for RELION's autopicking procedure on the full data sets. The selected particles were sorted by the particle sorting routine implemented in RELION 1.3 and manually inspected. All further processing was performed with RELION 1.3 (Extended Data Fig. 1b). As starting models for 3D classification, we used the available 10 Å map of apo Pol III (EMDB-1804; apo Pol III) and the 16.5 Å map of elongating Pol III (EMDB-1803) low-pass filtered to 60 Å. For the elongating Pol III, the initial data set of 800,000 particles was classified in 3D into 10 classes. Four classes were selected based on high particle abundance and occupancy of peripheral density at positions corresponding to the C82–C34–C31 and C53–C37 subcomplexes. The remaining 461,594 particles were subjected to a 3D sub-classification (for Pol III, 3D classification was initiated at this point with 515,397 particles). From 10 calculated classes, the most populated class with 121,241 particles for apo Pol III and 75,751 particles for elongating Pol III was further refined. We then employed RELION's movie processing routine (including the 'particle polishing' step) using all seven frames. The procedure deblurs images by particle-based motion correction and minimizes effects of radiation damage by B-factor like amplitude weighting of the subframes⁵¹. With the particle-polished data set, we performed another 3D classification using locally restrained alignment to resolve structural heterogeneity in the particle subset, which resulted in two classes with 68,818 and 52,423 particles for the apo Pol III data set and two classes at 49,543 and 26,208 particles for the elongating Pol III data set, respectively. Both apo Pol III classes were refined and finally, we obtained two reconstructions, class 1 ('closed clamp' apo Pol III) with a resolution

of 4.6 Å and class 2 ('open clamp' apo Pol III) at 4.7 Å. For the elongating Pol III, class 1 showed improved alignment and yielded a map with increased resolvability compared to the 75,751 particle reconstruction, whereas class 2 showed no apparent conformational difference to class 1, but showed reduced resolvability, corresponding to less well aligned particles. Class 1 was subsequently refined to a resolution of 3.9 Å according to FSC 0.143 criterion⁵². In order to estimate resolution, we compensated mask effects by performing the high-resolution noise substitution procedure within RELION⁵³ (Extended Data Fig. 1c). The resulting maps were post-processed in RELION by sharpening with an automatically calculated B-factor⁵⁴ of –136 Å² and –140 Å² for class 1 and 2 of apo Pol III and –100 Å² for elongating Pol III, respectively.

Local resolution was assessed using the tool RESMAP⁵⁵ (Extended Data Fig. 1c). The elongating Pol III map shows local resolution beyond 3.5 Å in the core and generally a uniform distribution of resolution between 3.5–4.6 Å for all subunits except the C34 WH3 (Extended Data Fig. 1c, 2, Extended Data Table 2). Both apo Pol III maps show stronger resolution differences between the core and peripheral subunits due to mobility of the heterotrimer and the stalk.

Model building and localization of subunits in the elongating Pol III density.

The building of initial models into the experimental density map was guided by homology models of Pol III subunits and crystal structures of archaeal RNA polymerase (PDB 4abc), Pol I (PDB 4c3i), Pol II (PDB 1wcm) as well as available crystal structures for the stalk (PDB 2ckz, 3ayh), the C82 homologue hRPC62 (PDB 2xub) and the TFIIF heterodimer (PDB 1f3u). All homology models were built using MODexplorer⁵⁶, HHsearch⁵⁷ and Modeller⁵⁸. Homology models of subunits C160 and C128 were built based on the Pol II structure, C11 based on the A12.2 subunit of Pol I, C82 on hRPC62 (PDB 2xub) and C34 WH3 domain based on an unrelated WH domain of highest sequence similarity (PDB 1ltd). The homology model of the stalk (C17–C25 dimer) was built based on the structures of C17–C25 dimer from *S. cerevisiae* (PDB 2ckz) and the HRDC (helicase and RNaseD C-terminal) domain of C17 taking the domain orientations from *S. pombe* C17–C25 structure (PDB 3ayh) that improved the fit with the electron microscopy map.

Manual model building and local real-space refinement was performed in COOT⁵⁹. For initial model building, the homology models were used to assemble a 15-subunit Pol III model consisting of all subunits except C34 and C31 which together with the above-mentioned crystal structures was placed into the elongating Pol III map by rigid body fitting. The fitted structures of individual subunits were used to aid *de novo* model building and re-building of reference models. Additionally, Xlink Analyzer⁶⁰ was used to display available lysine-lysine crosslinks and photo-crosslinks¹⁶ on the Pol III model, which allowed us to assign several peripheral densities to subunits C31, C34, C37 and C53. Our current models of apo and elongating Pol III account for most features observed in the experimental electron microscopy density maps, except for a few short stretches of density where unambiguous assignment to a subunit was not possible and two strong density peaks observed in both apo Pol III reconstructions and located close to the active site. We speculate that these densities might arise from variations in sample preparation and correspond to bound nucleotides and metal ions, although one of them could also result from a conformational switch of the rudder. There are six established Zn²⁺ binding sites located in the Pol III core subunits C160 (2), C128 (1), C11 (1), ABC10β (1) and ABC10α (1). We accounted for metal binding at these sites where the experimental density sufficiently supported the placement of metal ions.

To identify the position of the C34 WH3 domain, the homology model was fitted into the full density map at 5.5 Å using a systematic global search with the 'Fit In Map' tool of UCSF Chimera⁶¹. The fitting was performed using 100,000 random initial placements. These fits were clustered (leading to 30,000 unique fits) and scored by the normalized cross-correlation coefficient with the density map. The statistical significance of the scores was assessed as previously described⁶². Out of the statistically significant fits, the best scoring fit located C34 WH3 into a stretch of density unassigned by any other subunit next to subunit C82. The other significant fits corresponded to regions occupied by WH domains of C82 thus validating the ability of the systematic fitting procedure to locate WH domains in the experimental density. Although the WH1 and WH2 domains of C34 also fitted to this unassigned region, the positioning of WH3 domain was validated by cross-links to C82 and Consurf⁶³ that revealed a conserved surface of the WH3 domain towards C82 in contrast to C34 WH2 and WH1.

Refinement of elongating Pol III. To improve the model after initial model building, we performed automated real-space coordinate refinement against the elongating Pol III density map using a scripted workflow based on CCP4 and cctbx/PHENIX libraries^{64,65}. The sharpened experimental density map of elongating Pol III was used as the refinement target. Due to the resolution differences in the map we initially performed refinement of subcomplexes or individual subunits against map segments filtered at the appropriate resolution, ranging from 3.9 to 4.5 Å (Extended Data Table 1). To better account for the differences in map

resolution observed for different parts of the model, we calculated the local resolution distribution using RESMAP⁵⁵. We then computed a local mean resolution for each subunit by averaging all RESMAP voxels contained in a low-pass filtered volume generated from the model coordinates of this subunit (Extended Data Table 2). Segments comprising all voxels including and extending 3.5 Å outwards of the model coordinates were then carved from the elongating Pol III density map. A uniform isotropic B-factor of 50 Å² was assigned to all model atoms at the start of the refinement. The individual map segments and the corresponding coordinate models were centred in a cubic box of P1 symmetry with a cell dimension of 260.16 Å (240 × 240 × 240 pixels) to allow uniform grid sampling of model and experimental maps at the experimental pixel size. Coordinate refinement was performed by geometry-restrained real-space refinement based on gradient-driven minimization of a combined map and restraint target as implemented in cctbx/PHENIX up to the computed local mean resolution of each subunit. Grid searches were employed for automated identification of optimal refinement weights to balance the relative contribution of geometry and experimental restraints. Additional restraints were applied between hydrogen-bonded atoms in secondary structure elements. For the DNA–RNA of the transcription bubble, an initial model was obtained from the structure of a Pol II–Mediator complex³⁷ (PDB 4v1n) and restraints were generated with the LibG program distributed with CCP4/REFMAC (Fei Long, unpublished). The geometries of Zn²⁺ binding sites in C160, C128, C11 and ABC10β and ABC10α were restrained to reference values according to Harding^{66,67}.

Each round of model optimization was evaluated by computing the real-space cross-correlation (RSCC) between experimental map and a map calculated from the model coordinates. To this end, model maps were generated by calculating B-factor-weighted structure factors from the model coordinates (using electron atomic form factors⁶⁸) and computing the inverse Fourier transform. We refined individual isotropic atomic displacement parameters (ADPs) by optimizing the real-space correlation between model and experimental map. ADPs were obtained by fitting to the computed RSCC profile. The resulting B-factor distributions correlate well with local resolution estimates, with lowest B-factors in the Pol III core and higher B-factors in the peripheral subunits of the stalk (C25–C17) and the C53–C37 and C82–C34–C31 subcomplexes (Extended Data Fig. 4).

Automated real-space refinement cycles were alternated with manual model building in COOT⁵⁹. Manual model building was aided by experimental maps filtered at lower resolution and experimental maps that were re-sharpened by applying the structure factor amplitudes computed from the current model^{54,69}, which leads to decreased noise levels and increased visibility of structural features in some regions of the map, in particular in the peripheral Pol III subunits. Taking into account the refined B-factor distribution in the model, this map manipulation enhances structural features due to better correction of the Fourier amplitude fall-off resulting from experimental factors, but does not introduce model bias since experimental phases are used.

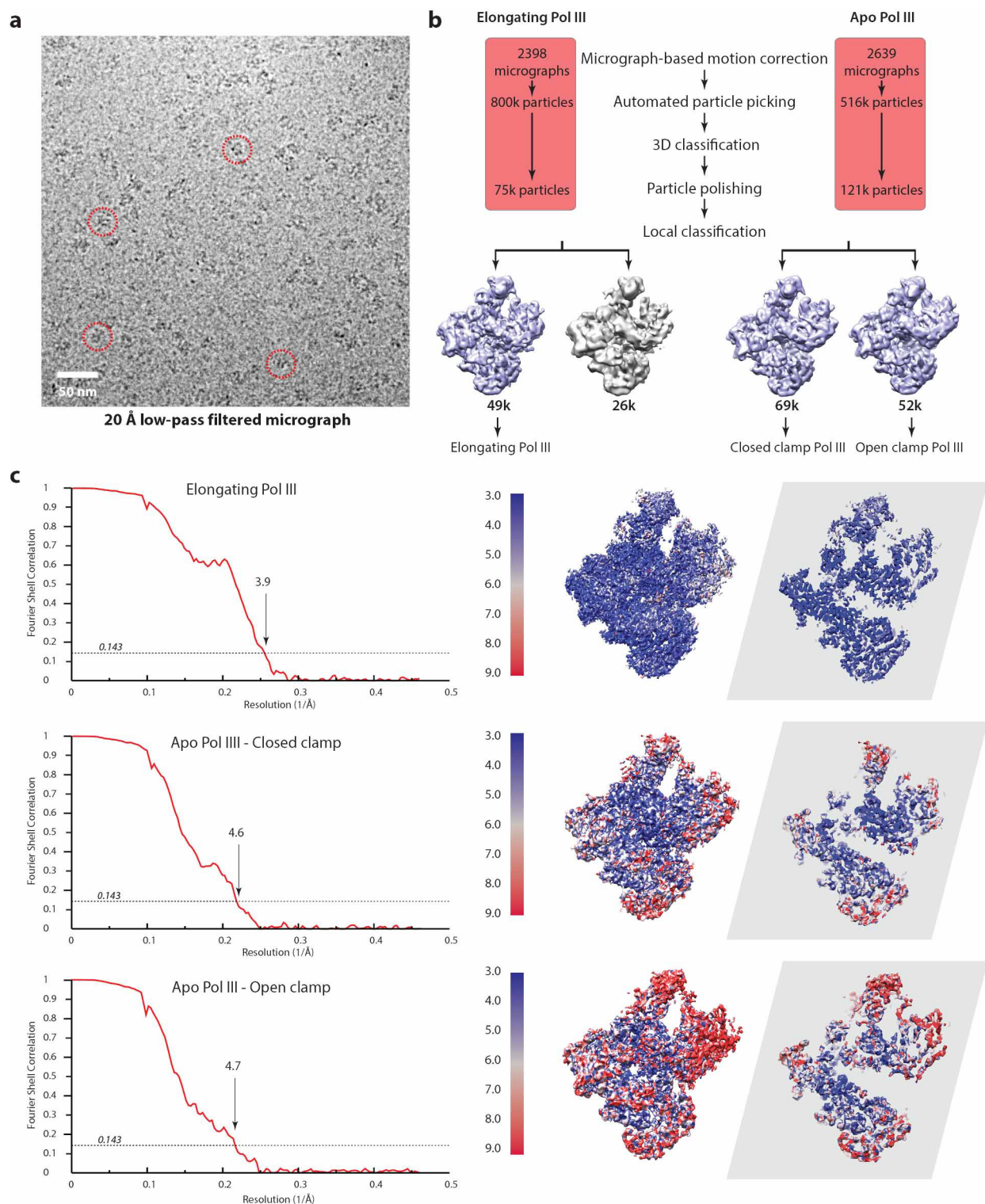
Following initial refinement of all individual subunits against the corresponding map segments, the entire elongating 17-subunit Pol III complex and the DNA–RNA transcription bubble was assembled and subjected to additional refinement against the full map reconstruction filtered at 3.9 Å resolution to account for inter-subunit interactions. The DNA–RNA model was not further refined at this stage. Since refinement target weights are optimized based on overall map resolution, restraint weighting can be suboptimal in regions of the map with a resolution lower than the average map resolution. To compensate for this effect in the full map refinement, we restrained peripheral subunits by an additional harmonic potential applied to the Cα positions, which was scaled relative to the average local resolution in this map region calculated as described above.

The Fourier shell correlation between model map and half-set 3D reconstructions was used to assess the possibility of overfitting⁷⁰. Briefly, the atoms in the model were randomly displaced by up to a maximum of 0.5 Å, followed by five cycles of real-space refinement against one of the half maps (work map) using the same protocol as described above. We then computed the FSC between the resulting model and the work map (FSC_{work}) as well as the cross-validated FSC between the refined model and the other half map not used in refinement (FSC_{test}). The close agreement between both curves for the elongating Pol III model indicates that no overfitting took place (Extended Data Fig. 4). We attribute the minor discrepancies in particular at low-resolution between FSC_{work}/FSC_{test} and the FSC between two independent half sets (Extended Data Fig. 1) to the incomplete model and solvent effects^{54,71}. The very good correlation in the high-resolution region beyond 6 Å provides support that our model accounts well for most of the defined density features observed in the experimental map. The quality of the final model was validated using MOLPROBITY⁷² and was found to range in the top percentiles for the corresponding resolution range.

Model building and refinement of apo Pol III (closed/open clamp conformation). The initial model for apo Pol III in the closed and open clamp conformations was obtained from the model coordinates of the individual subunits refined against the higher resolution map of elongating Pol III. The 10-subunit core, the C53–C37 heterodimer, the C82–C34–C31 heterotrimer and the stalk (C25–C17) were placed by rigid body fitting into the respective density maps. The C-terminal TFIIIS-like domain of C11, not visible in the elongating Pol III structure, was added to complete the model. The complete model was then refined against the respective maps filtered at 4.6/4.7 Å resolution. Sharpened maps for both closed and open clamp conformations of apo Pol III were used as the refinement target. Restraints on secondary structure and metal binding geometries were implemented as described for elongating Pol III. Automatic real-space refinement was performed as described above, with additional harmonic restraints on Cα positions weighted by the average local resolution to account for resolution anisotropy observed in both maps. Manual adjustments to the model were done in COOT; model assessment and validation were performed as described above. A summary of the refinement statistics for all three models can be found in Extended Data Table 1.

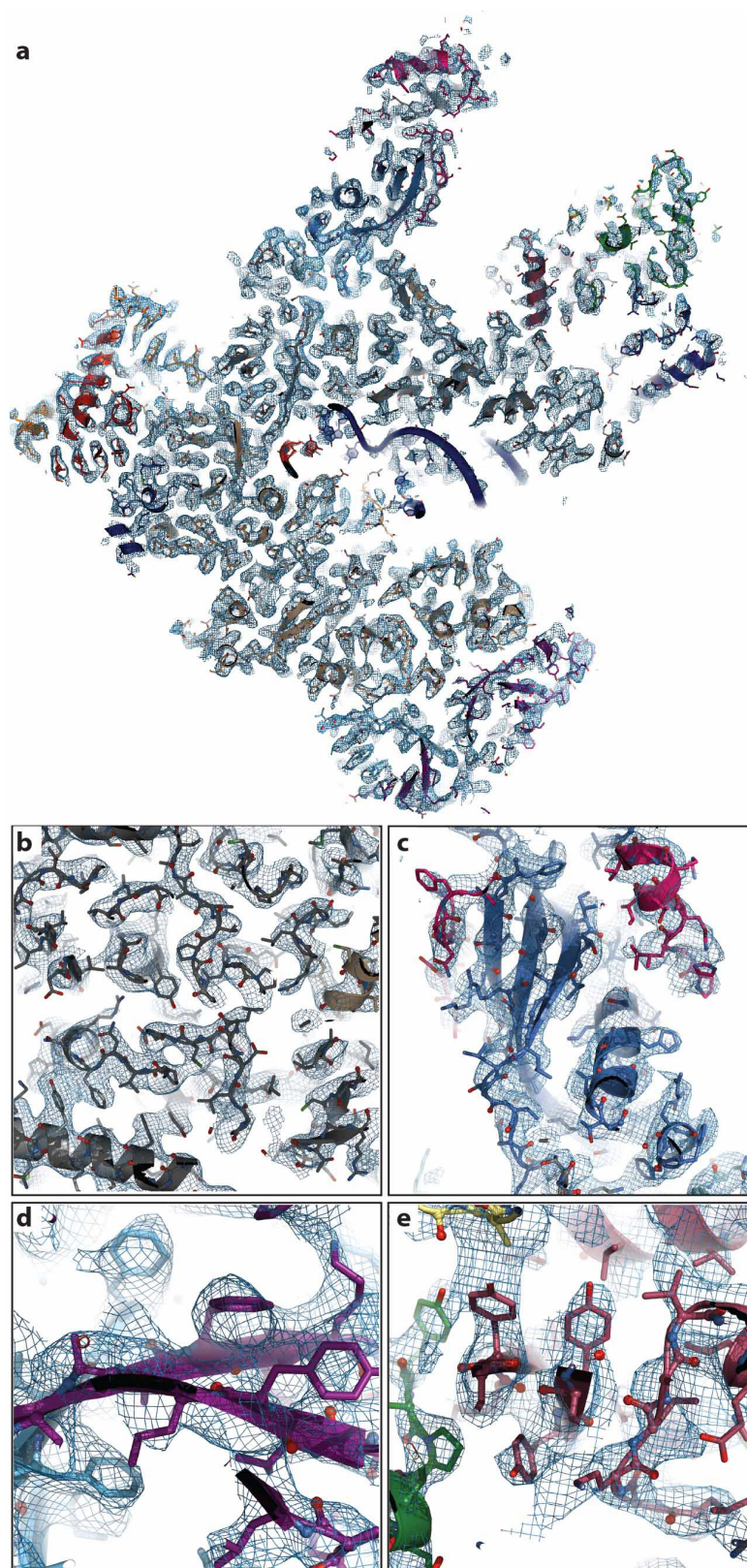
Figure preparation. Graphs and figures were prepared using XMGrace, Pymol⁷³ and UCSF Chimera⁶¹.

48. Li, X. *et al.* Electron counting and beam-induced motion correction enable near-atomic-resolution single-particle cryo-EM. *Nature Methods* **10**, 584–590 (2013).
49. Mindell, J. A. & Grigorieff, N. Accurate determination of local defocus and specimen tilt in electron microscopy. *J. Struct. Biol.* **142**, 334–347 (2003).
50. Ludtke, S. J., Baldwin, P. R. & Chiu, W. EMAN: semiautomated software for high-resolution single-particle reconstructions. *J. Struct. Biol.* **128**, 82–97 (1999).
51. Scheres, S. H. Beam-induced motion correction for sub-megadalton cryo-EM particles. *eLife* **3**, e03665 (2014).
52. van Heel, M. & Schatz, M. Fourier shell correlation threshold criteria. *J. Struct. Biol.* **151**, 250–262 (2005).
53. Chen, S. *et al.* High-resolution noise substitution to measure overfitting and validate resolution in 3D structure determination by single particle electron cryomicroscopy. *Ultramicroscopy* **135**, 24–35 (2013).
54. Rosenthal, P. B. & Henderson, R. Optimal determination of particle orientation, absolute hand, and contrast loss in single-particle electron cryomicroscopy. *J. Mol. Biol.* **333**, 721–745 (2003).
55. Kucukelbir, A., Sigworth, F. J. & Tagare, H. D. Quantifying the local resolution of cryo-EM density maps. *Nature Methods* **11**, 63–65 (2014).
56. Kosinski, J., Barbato, A. & Tramontano, A. MODexplorer: an integrated tool for exploring protein sequence, structure and function relationships. *Bioinformatics* **29**, 953–954 (2013).
57. Söding, J. Protein homology detection by HMM–HMM comparison. *Bioinformatics* **21**, 951–960 (2005).
58. Sali, A. & Blundell, T. L. Comparative protein modelling by satisfaction of spatial restraints. *J. Mol. Biol.* **234**, 779–815 (1993).
59. Emsley, P. & Cowtan, K. Coot: model-building tools for molecular graphics. *Acta Crystallogr. D* **60**, 2126–2132 (2004).
60. Kosinski, J. *et al.* Xlink Analyzer: software for analysis and visualization of cross-linking data in the context of three-dimensional structures. *J. Struct. Biol.* **189**, 177–183 (2015).
61. Pettersen, E. F. *et al.* UCSF Chimera—a visualization system for exploratory research and analysis. *J. Comput. Chem.* **25**, 1605–1612 (2004).
62. Bui, K. H. *et al.* Integrated structural analysis of the human nuclear pore complex scaffold. *Cell* **155**, 1233–1243 (2013).
63. Ashkenazy, H., Erez, E., Martz, E., Pupko, T. & Ben-Tal, N. ConSurf 2010: calculating evolutionary conservation in sequence and structure of proteins and nucleic acids. *Nucleic Acids Res.* **38**, W529–W533 (2010).
64. Adams, P. D. *et al.* PHENIX: a comprehensive Python-based system for macromolecular structure solution. *Acta Crystallogr. D* **66**, 213–221 (2010).
65. Winn, M. D. *et al.* Overview of the CCP4 suite and current developments. *Acta Crystallogr. D* **67**, 235–242 (2011).
66. Harding, M. M. Geometry of metal–ligand interactions in proteins. *Acta Crystallogr. D* **57**, 401–411 (2001).
67. Harding, M. M. Small revisions to predicted distances around metal sites in proteins. *Acta Crystallogr. D* **62**, 678–682 (2006).
68. Colliex, C. *et al.* in *International Tables of Crystallography* Vol. C (ed Prince, E.), 259–429 (International Union of Crystallography, 2006).
69. Sachse, C. *et al.* High-resolution electron microscopy of helical specimens: a fresh look at tobacco mosaic virus. *J. Mol. Biol.* **371**, 812–835 (2007).
70. DiMaio, F., Zhang, J., Chiu, W. & Baker, D. Cryo-EM model validation using independent map reconstructions. *Protein Sci.* **22**, 865–868 (2013).
71. Jiang, J. S. & Brünger, A. T. Protein hydration observed by X-ray diffraction. Solvation properties of penicillopepsin and neuraminidase crystal structures. *J. Mol. Biol.* **243**, 100–115 (1994).
72. Chen, V. B. *et al.* MolProbity: all-atom structure validation for macromolecular crystallography. *Acta Crystallogr. D* **66**, 12–21 (2010).
73. Schrödinger, L. L. C. *The PyMOL Molecular Graphics System, Version 1.3r1* (2010).



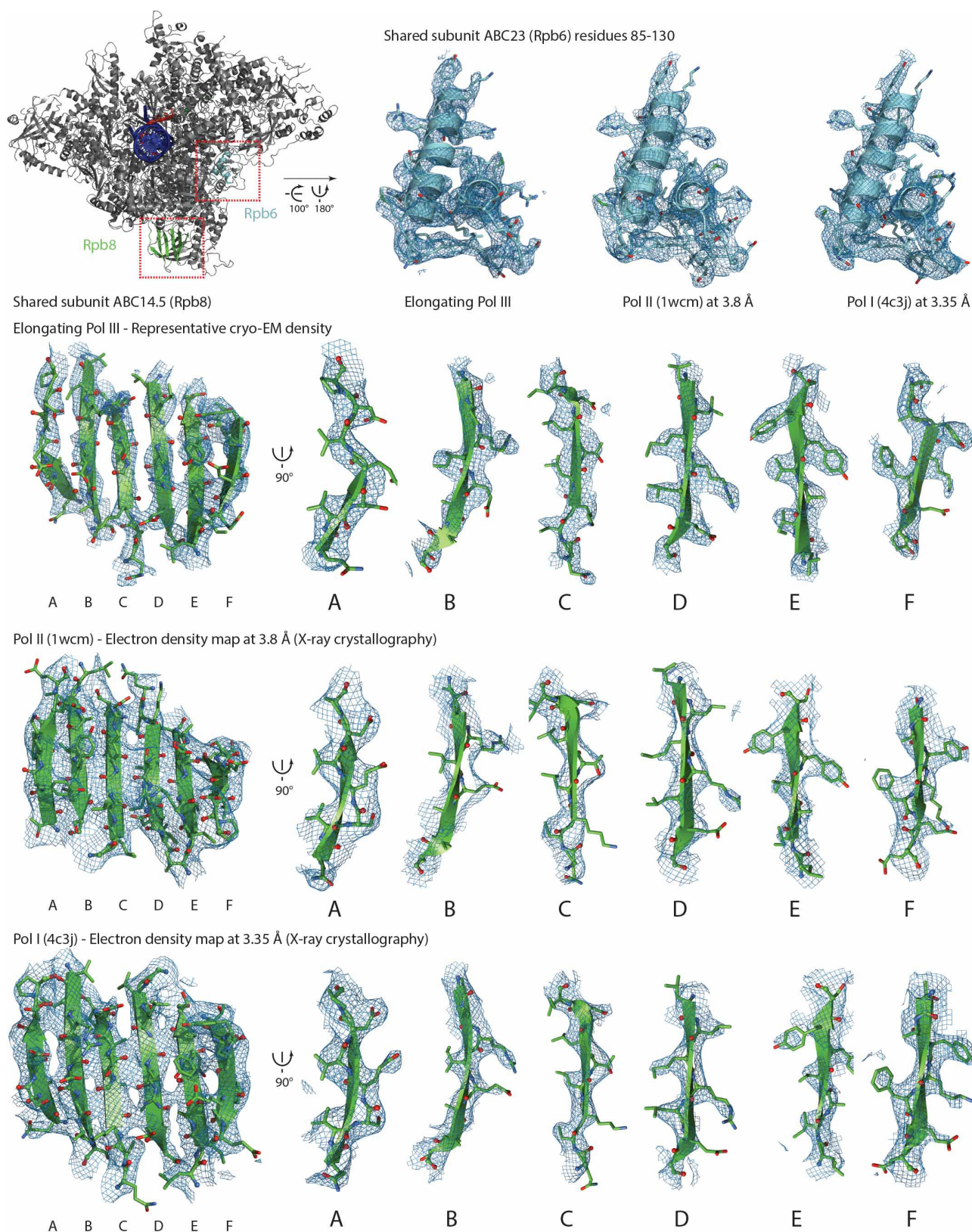
Extended Data Figure 1 | Pol III processing pipeline, Fourier-shell correlation curves and local resolution assessment. **a**, Exemplary micrograph of elongating Pol III. All micrographs were low-pass filtered for particle picking. **b**, General processing pipeline. The orange boxes display micrograph number and particles for elongating Pol III (left) and apo Pol III (right). The middle panel shows the general workflow that was followed for both data sets. For elongating Pol III (bottom left), a local classification step yielded one class with 49,543 particles (purple) that was subsequently refined and post-processed. For apo Pol III (bottom right), local classification diverged into two classes (purple) with 68,818 particles and 52,423 particles that were subsequently refined and post-processed. **c**, Fourier-shell correlation (FSC) and local resolution assessment with RESMAP⁵⁵. All FSC calculations were performed with two independent

half maps using RELION's masking procedure⁵³. The resolution for the elongating Pol III cryo-EM map (top panel) is 3.9 Å according to the FSC 0.143 criterion, indicated by the black dashed line. The two apo Pol III cryo-EM reconstructions have a resolution of 4.6 Å (closed clamp Pol III, middle panel) and 4.7 Å (open clamp Pol III, bottom panel) according to the FSC 0.143 criterion. Local resolution is displayed on the post-processed full maps (first image column on the right) and a cross-section representation (second image column on the right). In both apo Pol III reconstructions, the peripheral subcomplexes show a strong decay in resolution compared to the core. In the elongating Pol III reconstruction, the resolution is more uniformly distributed, indicating stabilization of peripheral subunits.



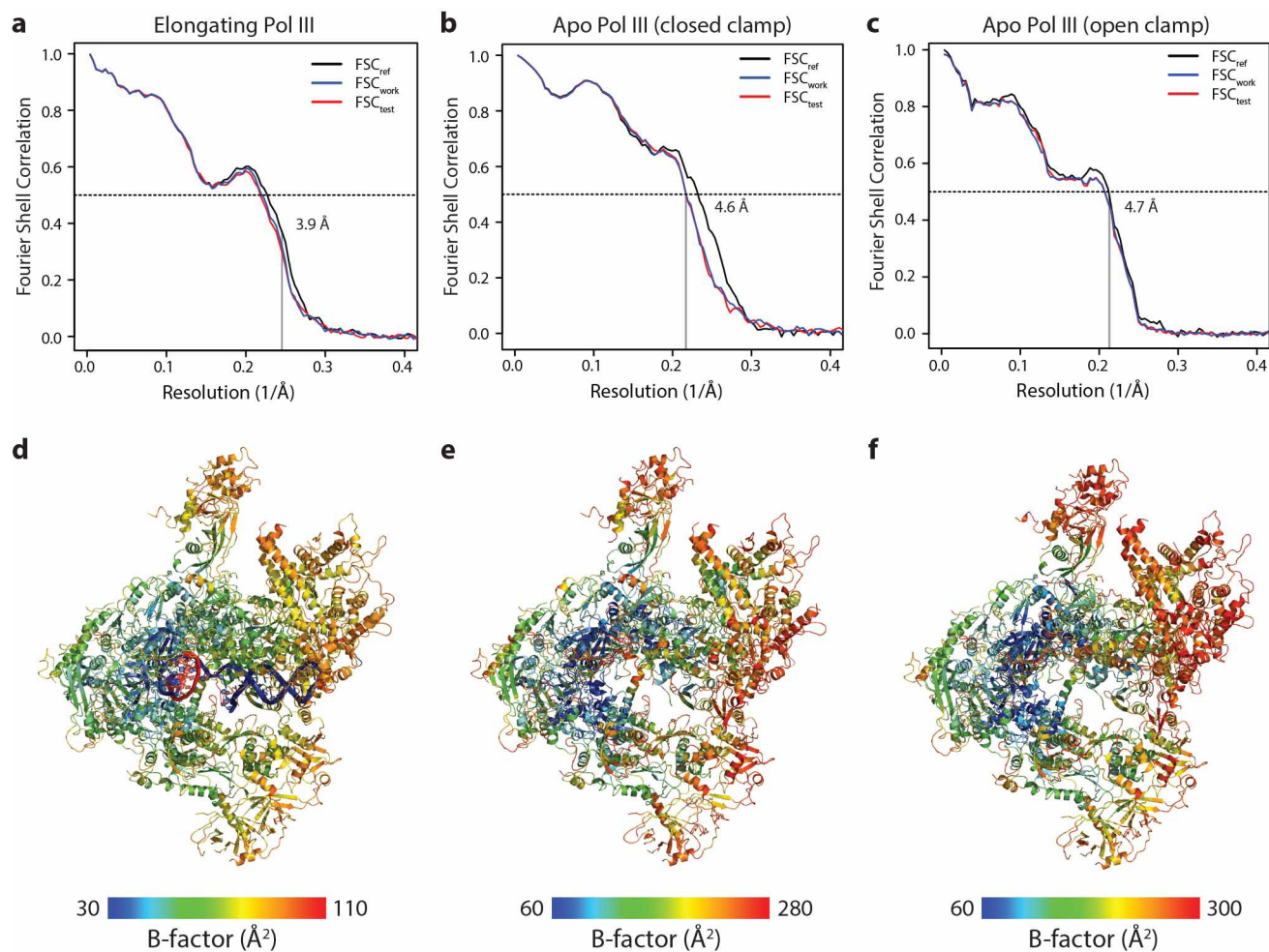
Extended Data Figure 2 | Representative sections of the cryo-EM density for elongating Pol III. **a**, Cross-section of elongating Pol III in ribbon and stick representation, embedded in the experimental density at 3.9 Å, displayed in dark blue. **b**, Section displaying the core subunits C160 (grey) and C128 (wheat) shown in stick and ribbon representation. The experimental density of the core (dark blue) is well defined and has

been filtered at 3.5 Å resolution for display. **c**, Section of stalk subunits C25 (blue) and C17 (pink). The estimated local resolution in this part is lower compared to the core (Extended Data Table 2). In **c**, **d** and **e**, the cryo-EM density is shown at 3.9 Å resolution. **d**, Section showing subunits C53 (blue) and C37 (purple). **e**, Close-up view of C82-WH1 (brown), C82-WH2 (green) and C31 (yellow) interface.



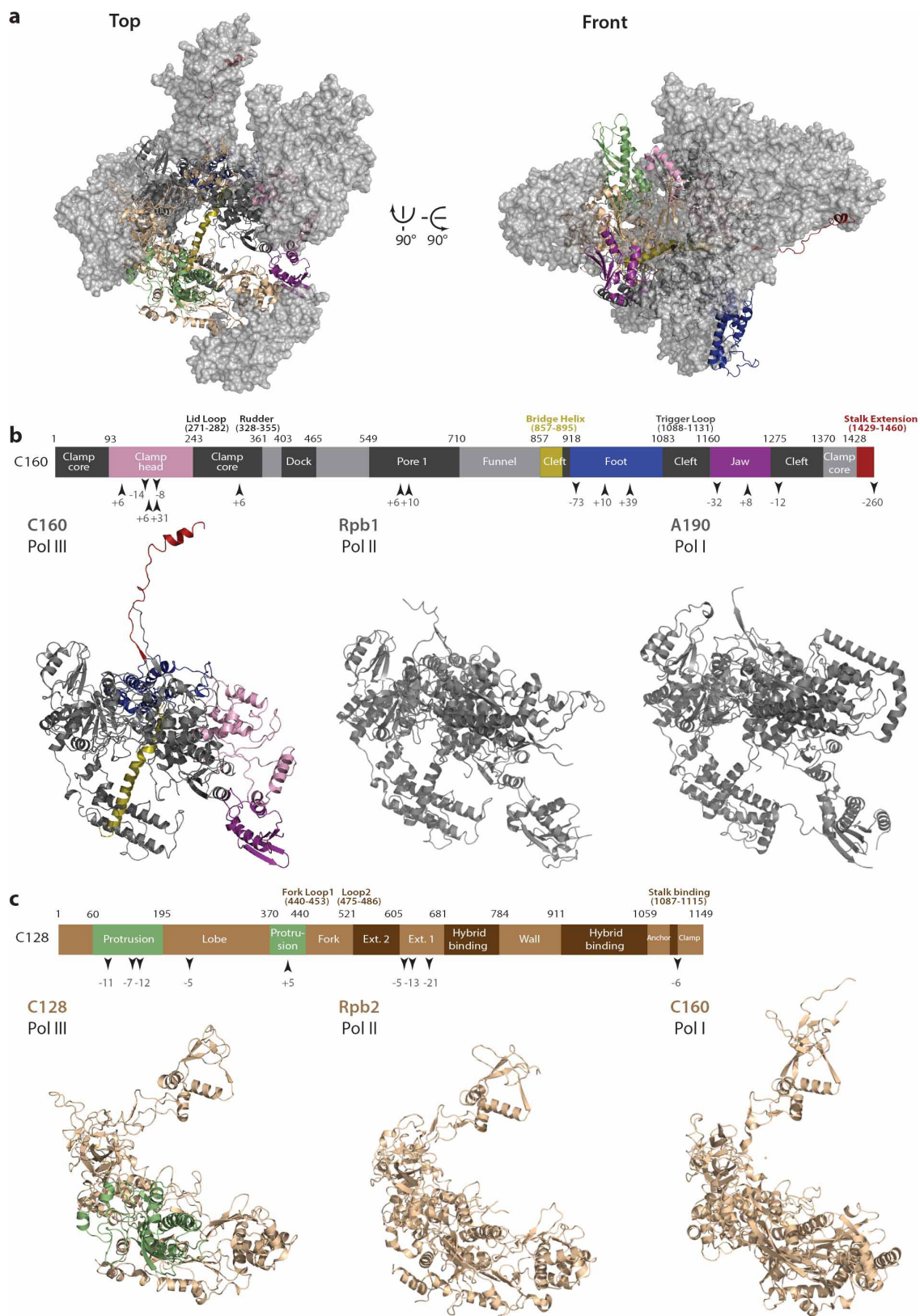
Extended Data Figure 3 | Comparison of electron microscopy densities with X-ray electron densities for shared subunits ABC23 (Rpb6) and ABC14.5 (Rpb8). Top left shows Pol III in front view, a stretch in ABC23 (cyan) and ABC14.5 (green) is coloured. The red boxes indicate the regions that are enlarged in the neighbouring panels. Corresponding density is displayed in tungsten. Models of Pol II and Pol I at nominally higher resolution are available, but for better comparison models in a

similar resolution range are shown. For the $2F_o - F_c$ electron density maps obtained by X-ray crystallography a threshold of 1σ was used for display. The top right shows three close-up views of the shared subunit ABC23 from elongating Pol III, Pol II (PDB 1wcm) and Pol I (PDB 4c3j). The bottom panels show 6 strands of shared subunit ABC14.5. Front view of the β -sheet and orthogonal views of individual strands in elongating Pol III, Pol II (PDB 1wcm) and Pol I (PDB 4c3j).



Extended Data Figure 4 | Model validation and temperature factor distribution of atomic models. **a–c**, FSC curves calculated between the refined atomic model and the half map used in refinement (FSC_{work}) are shown in blue, those calculated between the refined atomic model and the second half map not used for refinement (FSC_{test}) in red. Vertical lines mark the regular FSC 0.143 cutoff and the resolution target used in refinement as shown. Close agreement between FSC_{work} and FSC_{test} and the absence of a sharp drop beyond the refinement target resolution

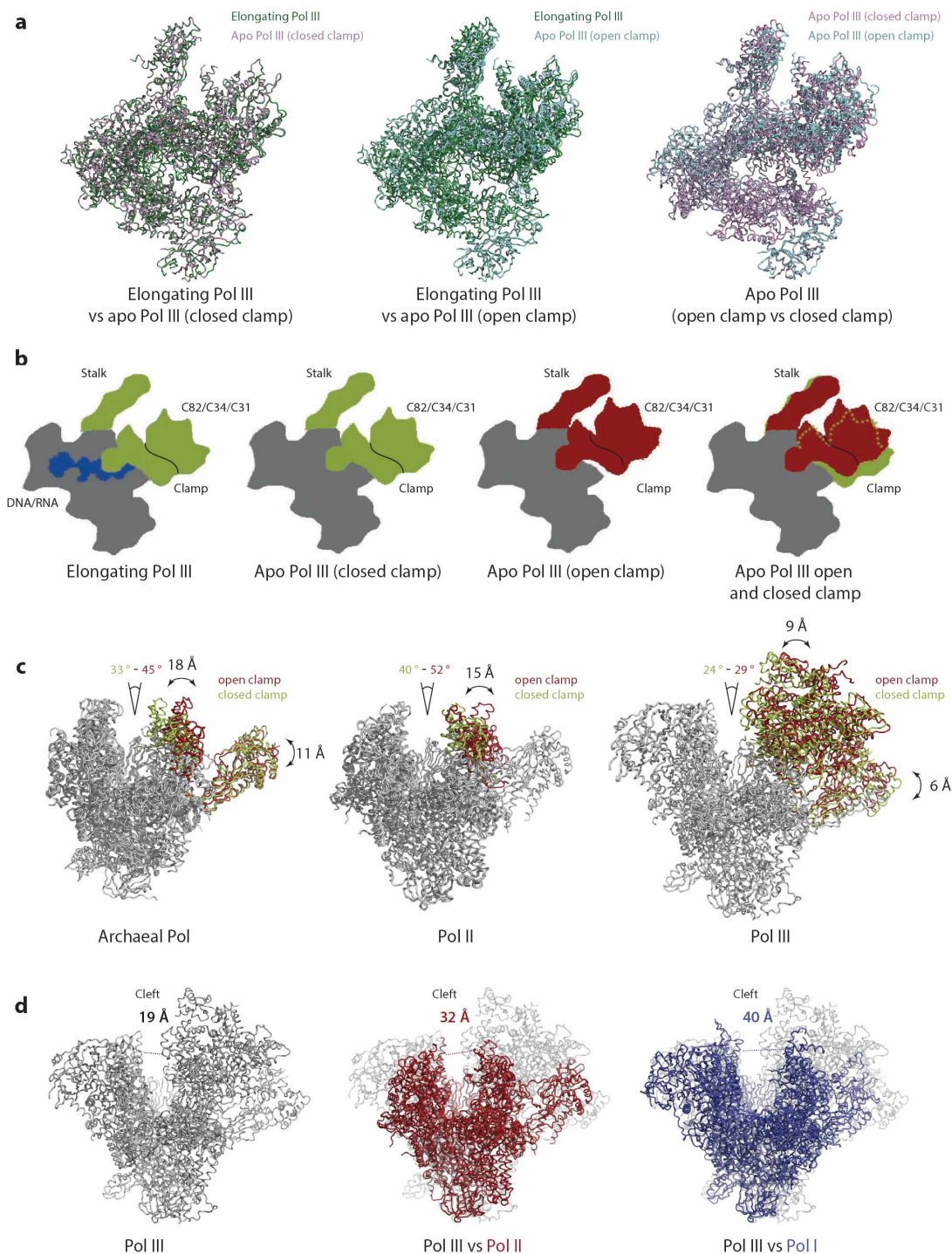
indicate that no overfitting took place. The respective FSC between the refined atomic model and the map obtained from 3D reconstruction using the entire data set (FSC_{ref}) is also shown (black). **d, e**, Atomic B-factor distributions mapped on ribbon representations of elongating and apo Pol III. The overall distribution and relative differences between core and peripheral subunits for the different models correlate well with the distribution of local resolution (Extended Data Fig. 1).



Extended Data Figure 5 | Pol III-specific features of subunits C160 and C128 and comparison to the homologous Pol II and Pol I subunits.

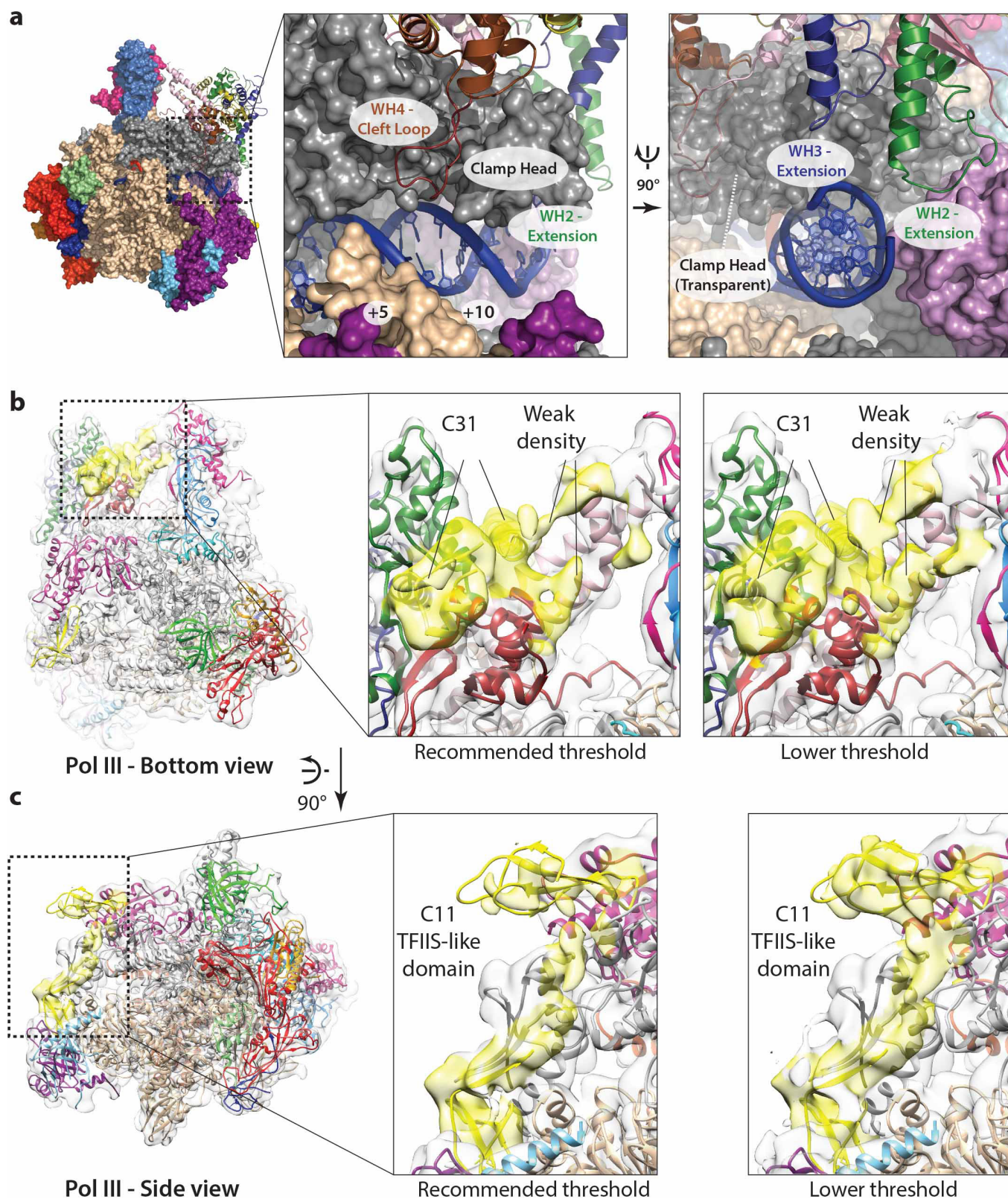
a, Top (left) and front (right) view of Pol III, with subunits C160 and C128 displayed in ribbon representation and the other subunits in surface representation (grey). Coloured stretches highlight characteristic features denoted in **b**. **b**, Bar diagram shows the domain organization of Pol III C160. Arrows and corresponding numbers below the bar diagram indicate

insertions and deletions of five or more residues in Pol III relative to Pol II subunit Rpb1 as indicated by structure-based alignment. Coloured regions are also shown in Pol III subunit C160 (lower panel, left) and in **a**. Lower panel middle and right show Pol II Rpb1 and Pol I A190 subunits, respectively. **c**, Same as in **b** for Pol III subunit C128. Insertions and deletions compared to Pol II subunit Rpb2 are displayed in the box diagram.



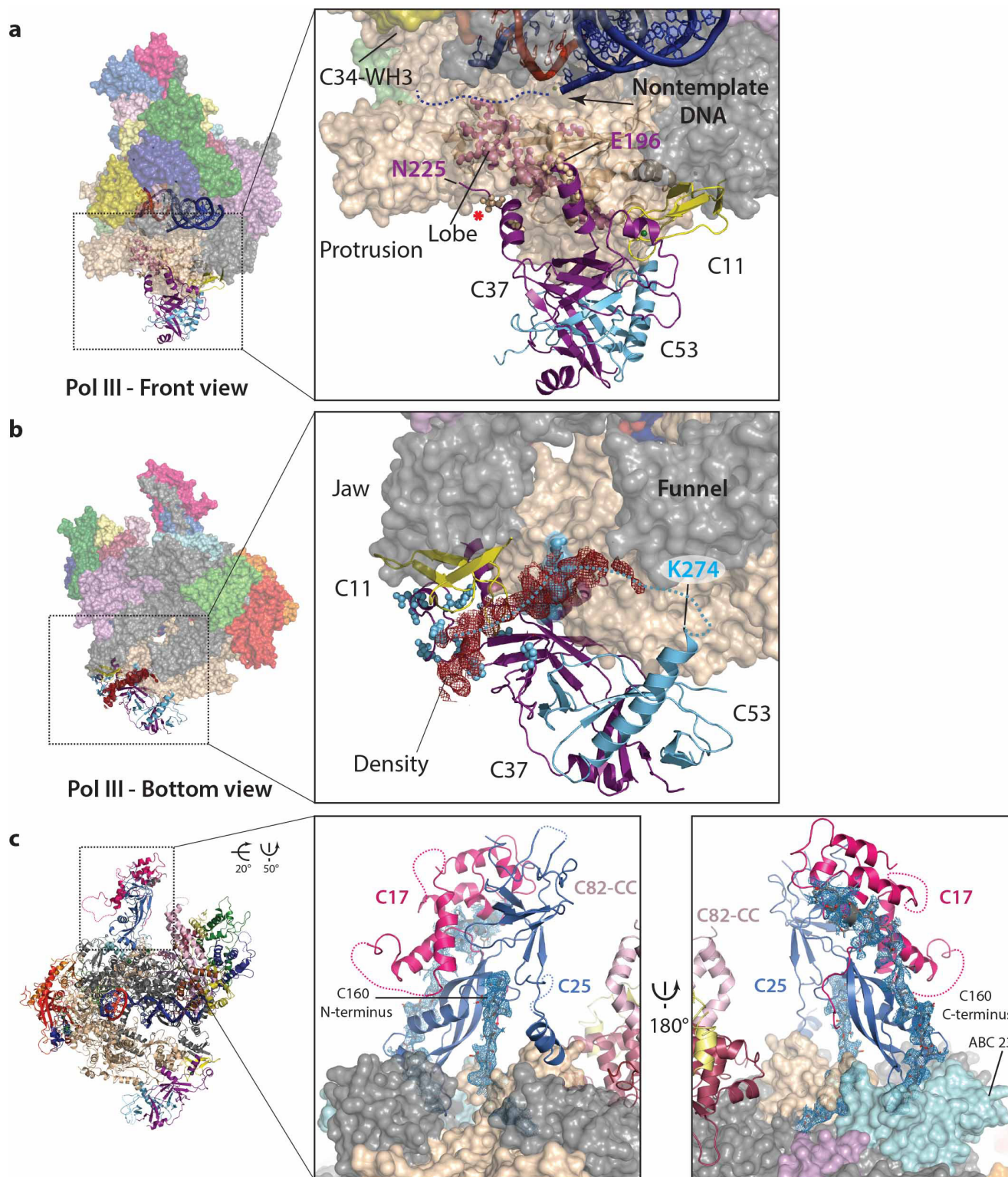
Extended Data Figure 6 | Open and closed clamp conformation in Pol III compared to other RNA polymerases. **a**, Top view of aligned elongating Pol III and apo Pol III (left panel, closed clamp; middle panel, open clamp) and both closed clamp and open clamp apo Pol III conformations (right panel). r.m.s.d. values (core-heterodimer:all) for elongating Pol III – apo Pol III (closed clamp) (0.43 Å_{4,813} C α atoms aligned), elongating Pol III – apo Pol III (open clamp) (0.71 Å_{3,496} C α atoms aligned; 2.73 Å_{4,795} C α atoms aligned) and both apo Pol III open and closed clamp (0.71 Å_{3,540} C α atoms aligned; 2.71 Å_{4,829} C α atoms aligned) demonstrate the similarity between closed clamp apo Pol III and elongating Pol III conformations. **b**, Schematic representation of Pol III in top view showing the conformational changes of clamp head, heterotrimer and stalk. The closed clamp conformation (elongating Pol III and closed clamp apo Pol III) is displayed in red, the open clamp conformation (open clamp apo Pol III) in green. The DNA–RNA duplex is shown in blue, the core and heterodimer in grey. **c**, Front view on open and closed

clamp conformations in other RNA polymerases. The closed clamp state (green) and open clamp state (red) is indicated for archaeal polymerase (left panel, PDB 4ayb and 4qiw), for Pol II (middle panel, PDB 1wcm and 1twf) and for Pol III (right panel). Green and red angles describe the cleft opening in the closed and open clamp conformations. Black arrows and corresponding values indicate the relative distance of the subunits between the two conformations. **d**, Front view of apo Pol III closed clamp (left panel), apo Pol III closed clamp vs apo Pol II (middle panel, Pol II (PDB 1wcm) in red) and apo Pol III closed clamp vs apo Pol I (right panel, Pol I (PDB 4c3i) in blue). The cleft opening is indicated by a dashed line and the C α –C α distance across the cleft (black for Pol III, red for Pol II and blue for Pol I). However, some of the observed differences in cleft width between Pol I, Pol II and Pol III might also reflect differences between conditions of cryo-EM and crystal structures as well as different packing contacts in the crystals.



Extended Data Figure 7 | Pol III-specific subunits C82, C31 and C11.
a, Left panel: overall surface representation of Pol III with the C82–C34–C31 heterotrimer in ribbon representation. Right panels: two enlarged and orthogonal views of the region marked with a dotted black square. In subunit C82 WH4 inserts in the DNA binding cleft passing through a canyon in the clamp head. WH2 and WH3 extensions reach over the clamp head and are positioned in close proximity to downstream DNA.
b, Ribbon model of Pol III fitted into the electron microscopy density of the open clamp apo Pol III filtered at 6 Å resolution. For C31, additional

density is visible in the cavity between the stalk and the heterotrimer, as shown in the top right panel. The described densities are also present in the closed clamp apo Pol III and the elongating Pol III reconstructions. No attempts were made to fit atomic models into these densities.
c, Electron microscopy density of the C11 TFIIS-like domain at 6 Å resolution as observed in the open clamp apo Pol III reconstruction. The left panel shows a side view of Pol III, the middle and right panels show close-ups at two different density thresholds.



Extended Data Figure 8 | C53–C37 heterodimer and stalk subunits C25–C17. **a**, Visualization of the photo-crosslinks between C53–C37 heterodimer and subunit C128. Pol III is shown in surface, C53–C37 and C11 in ribbon representation. In addition, the C128 lobe is shown in cartoon representation (small inset). Purple spheres on the lobe indicate residues that photo-crosslink to C37 (ref. 13), beige spheres on C37 indicate residues that photo-crosslink to C128 (ref. 13). The dashed line marks the tentative path of the non-template DNA strand. The experimental photo-crosslinks fit well to the cryo-EM structure. The C37 loop is disordered between Glu196 and Asn225, although photo-crosslinks indicate that this region is in close proximity to the lobe and the non-template DNA strand. **b**, Bottom view of Pol III in surface representation,

with C53–C37 and C11 shown in ribbon representation. The black dotted square indicates the enlarged area in the centre of the image (small inset). The red density (shown at 4.5 Å) was not of sufficient quality to build an atomic model. However, photo-crosslinks from C37 and C128 to C53 (blue spheres on C37 ribbon and C128 surface mark crosslink positions)¹³ indicate that C53 N-terminal residues are located in this region. **c**, Stalk anchoring with C160 extensions. Top view (left panel) and bottom view (right panel) of the stalk subunits C17 (magenta), C25 (blue) and the C160 extensions (grey). Electron microscopy density corresponding to the C160 N- and C-terminal extensions is shown in tungsten blue. Individual entities and subunits are labelled.

Extended Data Table 1 | Refinement statistics

	Elongating Pol III	Apo Pol III (closed clamp)	Apo Pol III (open clamp)
Model composition			
No. of chains	17+3	17	17
Non-hydrogen atoms	39276	38677	38427
Protein residues	4839	4882	4845
Nucleic acid	47	--	--
Ligand (Zn ²⁺)	6	6	6
Refinement			
PDB ID	5fj8	5fj9	5fja
Resolution (Å)	260.2-3.9	260.2-4.6	260.2-4.7
Map sharpening B-factor (Å ²)	-100	-136	-140
Average B-factor (Å ²)			
<i>Protein</i>	64.9	161.8	182.0
<i>Nucleic acid</i>	76.3	--	--
<i>Ligand (Zn²⁺)</i>	58.6	62.4	107.9
Molprobity score	2.6	2.58	2.48
Clashscore (all atoms)	14.5	13.41	13.84
Rotamer outliers (%)	2.00	2.08	1.5
Ramachandran statistics			
Favored (%)	82.46	82.52	82.58
Disallowed (%)	1.15	1.23	1.03
RMS (bonds, Å)	0.0032	0.0032	0.0030
RMS (angles, °)	1.03	1.01	0.89
Nucleic Acid			
Correct sugar puckers (%)	91.5	--	--
Good backbone conform. (%)	68.7	--	--

Extended Data Table 2 | Model statistics for elongating Pol III

Subunit	Protein	Chain ID	Mw (kDa)	No. of residues	Residues built	Chain breaks	All-atom clashscore	Molprobability score	Average B-factor (\AA^2)	Local resolution (\AA)
Core										
<i>RPC1</i>	C160	A	162.3	1460	1422 (97.4%)	3	10.42	2.24	56.35	3.8
<i>RPC2</i>	C128	B	129.5	1149	1115 (97.0%)	--	12.61	2.40	60.10	3.8
<i>RPC40</i>	AC40	C	37.7	335	335 (100%)	--	10.60	2.40	60.42	3.8
<i>RBP5</i>	ABC27	E	25.1	215	215 (100%)	--	16.07	2.81	67.97	4.1
<i>RBP6</i>	ABC23	F	17.9	155	83 (53.5%)	--	3.67	2.34	57.97	3.6
<i>RBP8</i>	ABC14.5	H	16.5	146	140 (95.9%)	1	9.05	2.15	62.64	4.2
<i>RPC11</i>	C11	I	12.5	110	43 (39.1%)	--	16.00	2.73	73.40	4.3
<i>RBP10</i>	ABC10 β	J	8.3	70	68 (97%)	--	5.40	2.39	56.79	3.6
<i>RPC19</i>	AC19	K	16.1	142	101 (71.1%)	--	8.85	2.41	59.38	3.7
<i>RPC10</i>	ABC10 α	L	7.2	70	46 (65.7%)	--	12.13	2.65	67.80	4.2
Stalk										
<i>RPC9</i>	C17	D	18.6	161	119 (73.9%)	2	15.82	2.51	73.39	4.4
<i>RPC8</i>	C25	G	24.3	212	191 (90.1%)	2	16.86	2.67	70.03	4.3
Heterotrimer										
<i>RPC3</i>	C82	O	74.0	654	539 (82.4%)	2	15.99	2.86	73.08	4.5
<i>RPC6</i>	C34	P	36.1	317	89 (28.1%)	2	26.41	3.54	75.84	5.3
<i>RPC7</i>	C31	Q	27.7	251	63 (25.1%)	2	10.13	2.13	76.61	4.6
Heterodimer										
<i>RPC5</i>	C37	M	32.1	282	164 (58.2%)	1	11.72	2.59	74.18	4.3
<i>RPC4</i>	C53	N	46.7	422	110 (26.1%)	1	12.10	2.98	71.51	4.2
RNA	RNA	R		18	9 (50.0%)	--			75.00	3.9
DNA	Non-Template	S		38	15 (39.5%)	--			75.91	3.9
DNA	Template	T		38	23 (60.5%)	--			78.03	3.9